

A gradient smoothing method (GSM) based on strong form governing equation for adaptive analysis of solid mechanics problems

Jian Zhang^{a,*}, G.R. Liu^{b,c}, K.Y. Lam^d, Hua Li^d, G. Xu^e

^aDepartment of Civil Engineering, National University of Singapore, 1 Engineering Drive 2, Singapore 117576, Singapore

^bCentre for ACES, Department of Mechanical Engineering, National University of Singapore, 10 Kent Ridge Crescent, Singapore 119260, Singapore

^cSingapore-MIT Alliance (SMA), E4-04-10, 4 Engineering Drive 3, Singapore 117576, Singapore

^dSchool of Mechanical and Aerospace Engineering, Nanyang Technological University, 50 Nanyang Avenue, Singapore 639798, Singapore

^eInstitute of High Performance Computing, 1 Science Park Road, #01-01 The Capricorn Singapore Science Park II, Singapore 117528, Singapore

ARTICLE INFO

Article history:

Received 22 September 2007

Received in revised form 6 May 2008

Accepted 22 June 2008

Available online 9 August 2008

Keywords:

Numerical methods

Gradient smoothing method (GSM)

Strong form

Residual

Error indicator

Adaptive analysis

ABSTRACT

A gradient smoothing method (GSM) based on strong form of governing equations for solid mechanics problems is proposed in this paper, in which gradient smoothing technique is used successively over the relevant gradient smoothing domains to develop the first- and second-order derivative approximations by calculating weights for a set of field nodes surrounding a node of interest. The GSM is found very stable and can be easily applied to arbitrarily irregular triangular meshes for complex geometry. Unlike other strong form methods, the present method has excellent stability that is crucial for adaptive analysis. An effective and robust residual based error indicator and simple refinement procedure using Delaunay diagram are then implemented in our GSM for adaptive analyses. The reliability and performance of the proposed GSM for adaptive procedure are demonstrated in several solid mechanics problems including problems with singularities and concentrated loading, compared with the well-known finite element method (FEM).

© 2008 Elsevier B.V. All rights reserved.

1. Introduction

With the rapid development of computer technology in the past few decades, a broad range of numerical methods have been developed for different types of problems and achieved great success, e.g., the finite element method (FEM), finite difference method (FDM), finite volume method (FVM) and recently the meshfree methods [1–3]. In advanced design of products of high precision, adaptive analysis is becoming an important tool in practical numerical computations [4]. It is a fundamental tool to obtain numerical solutions with a desired accuracy. In an adaptive procedure, there are three essential ingredients: (1) an effective and stable numerical method for arbitrary problem domains and irregular meshes; (2) a tool for estimating the error of the numerical solution; and (3) an algorithm to refine the problem domain. The first ingredient is a prerequisite, without which an adaptive process will break down. The error estimator is crucial in assessing the local and global errors in the numerical solution at a stage of analysis, whereby a decision can be made on whether a refinement is required. The third is performed according to the error information provided by the error estimate.

The effectiveness and efficiency of all these three pieces of techniques are critical to the performance of an adaptive analysis. To conduct a posteriori error estimation, two values of a quantity—a computed value and a reference value—are usually required. The first is the raw data of the numerical solution while the second is derived from the raw data via postprocessing (smoothing or projection). In FEM, it is well known that the raw stresses (or derivatives) do not possess inter-element continuity and have a low accuracy at nodes and element boundaries. The improved values are obtained by smoothing the inter-element discontinuity. The difference between the raw and improved values forms a basis for error estimation in FEM solution. Detailed descriptions of this approach can be found in FEM literatures, e.g., by Zienkiewicz [5].

To establish an adaptive finite element procedure, one of the most important components is a robust automatic mesh generation scheme. However, to develop and implement automatic mesh generators with good control of element size and shape is not an easy task. During the last decade, many research efforts have been devoted to this area [6,7] and yet it still remains an active research topic in computational mechanics and geometry. Currently, automatic mesh generators of triangular elements for complex geometry are available. Unfortunately, the triangular elements used in FEM are known to be 'too stiff' and inaccurate. Compared with the finite element method, the meshfree methods enjoy much more flexibility

* Corresponding author. Tel.: +65 6516 4515; fax: +65 6779 1635.

E-mail address: cvezj@nus.edu.sg (J. Zhang).

in model generation since they can approximate field variables entirely based on a group of discrete nodes and require no predefined node connectivity. For meshfree methods that require background cells, triangular cells can be used, which will not affect the accuracy in the solutions. Nodes used in many meshfree methods can be irregular or unstructured. Nodes can be quite freely inserted or deleted without worrying too much about the connectivities. Therefore, the meshfree methods are particularly attractive for the development of adaptive strategies. Several adaptive procedures and error estimates for meshfree methods have been proposed. Duarte and Oden [8] derived an error estimator for the h - p cloud methods that involves only the computation of interior residuals and residuals where Neumann boundary conditions are prescribed. Liszka et al. [9] built discrete models of boundary-value problems with different adaptive strategies. Chung et al. [10], Gavete et al. [11] and Lee and Zhou [12] proposed adaptive refinement procedures and error indicators for the element-free Galerkin (EFG) method. Park et al. [13] developed a posteriori error estimates and an adaptive refinement scheme of first-order least-squares meshfree method.

Among these developed adaptive meshfree methods, the weak form methods, e.g., EFG method, are most well established. The solutions of weak form methods are usually very stable. In contrast, the development of meshfree strong form methods is rather sluggish. Available literatures for the meshfree strong form methods are still very limited. However, the meshfree strong form method possesses many good features for adaptive analysis due to its simplicity. The strong formulation is much simple, straightforward and easy to implement. The meshfree strong form method is considered a truly meshfree method as it does not even require background cells that are needed in weak form method for integration. Such distinct features facilitate the refinement or coarsening scheme in the adaptive scheme. Moreover, unlike weak form methods, strong form methods need no integration and hence no mapping is needed.

However, the instability problem has been a key factor that limits the application of meshfree strong form methods that use local nodes. Researchers have introduced several stabilization schemes [14,15], in which stabilization factors need to be determined. Many efforts have been devoted to point collocation methods based on reproducing kernel approximations [16–18]. Currently, most of the 'full-proof' strong form method is still very much relying on the structured grid and restricted regular domain. Although methods like generalized finite difference method (GFD) [19,20] can be used for irregular domain and unstructured grid, a proper stencil (node selection) is somehow still needed for function approximation. Such inconvenience procedures give difficulties to the strong form method in the adaptive process. In addition, since nodal distribution during the adaptation can become highly irregular, a 'proper' stencil can be costly and difficult to form.

In this paper, a gradient smoothing method (GSM) is proposed based on strong form governing equations. Gradient smoothing technique is utilized to construct first- and second-order derivative approximations by systematically computing weights for a set of nodal points surrounding a node of interest. Three types of different domains for the gradient smoothing operations are devised. The strong form of governing equations is directly discretized at nodes using gradient smoothing repeatedly over relevant gradient smoothing domains. These computations can be easily performed based on an irregular triangular mesh that can be generated automatically for complex geometries. The stencil analyses of weighting coefficients have been conducted for the Laplace operators, and favorable weight distributions are found. The proposed GSM can effectively overcome the instability issue, while retaining the strong form feature of simplicity in formulation procedures which is particularly suitable for adaptive analysis.

A residual based error indicator is then adopted in our GSM for adaptive analyses. By evaluating the residual of the governing equa-

tion for each triangular cell in the domain, error indicator effectively identifies the necessary regions to be refined. Simple refinement procedure using Delaunay diagram is adopted in the adaptive scheme. Additional nodes can be inserted into the domain easily without worrying about the nodal connectivity and remeshing the domain.

The layout of this paper is as follows: Section 2 theoretically formulates the GSM. In Section 3, a brief description of a posteriori error indicator based on residual of the governing equation is provided. Section 4 illustrates the capabilities of the present method through some numerical examples including different levels of stress concentration. The performance of the proposed strategy is also assessed by comparing the convergence rate obtained with those by uniform refinement. Conclusions are stated in Section 5.

2. Gradient smoothing method (GSM)

2.1. Gradient smoothing

Consider a two-dimensional elastostatic problem governed by the following equilibrium equation in the domain Ω :

$$\mathbf{L}\mathbf{u} = \mathbf{f} \quad \text{in } \Omega \quad (1)$$

with essential (Dirichlet) boundary conditions

$$\mathbf{u} = \bar{\mathbf{u}} \quad \text{on } \Gamma_u \quad (2)$$

and natural (Neumann) boundary conditions

$$\mathbf{B}\mathbf{u} = \mathbf{g} \quad \text{on } \Gamma_t \quad (3)$$

where \mathbf{L} , \mathbf{B} are the differential operators, \mathbf{u} is the field variable and \mathbf{f} , \mathbf{g} are external force vectors. Eq. (3) is derived using Cauchy's formula

$$\sigma_{ij}n_j - t_i = 0 \quad (4)$$

In the strong form methods, Eqs. (1)–(3) are directly collocated at the field nodes in the problem domain and on the boundaries, respectively. The discretized system governing equations are given as follows:

$$L(u_i) = f_i \quad \text{in } \Omega \quad (5)$$

with Dirichlet boundary conditions

$$u_i = \bar{u}_i \quad \text{on } \Gamma_u \quad (6)$$

and Neumann boundary conditions

$$B(u_i) = g_i \quad \text{on } \Gamma_t \quad (7)$$

where subscript "i" denotes the collocation point.

The governing equations (5)–(7) can be collocated at their corresponding field nodes then be assembled and expressed in the following matrix form:

$$\mathbf{K}\mathbf{U} = \mathbf{F} \quad (8)$$

where \mathbf{K} is the stiffness matrix, \mathbf{F} is the force vector and \mathbf{U} is the vector of unknown nodal values. Note that the stiffness matrix resulted from collocation is generally unsymmetric. The vector of unknown nodal values can be easily solved as

$$\mathbf{U} = \mathbf{K}^{-1}\mathbf{F} \quad (9)$$

if \mathbf{K} is not singular and well-conditioned.

In the present method, the problem domain Ω is discretized by triangular cells as shown in Fig. 1. For the i -th node, a smoothing domain Ω_i is generated by sequentially connecting the centroids with mid-edge points of surrounding triangular cells. Γ_i is the boundary

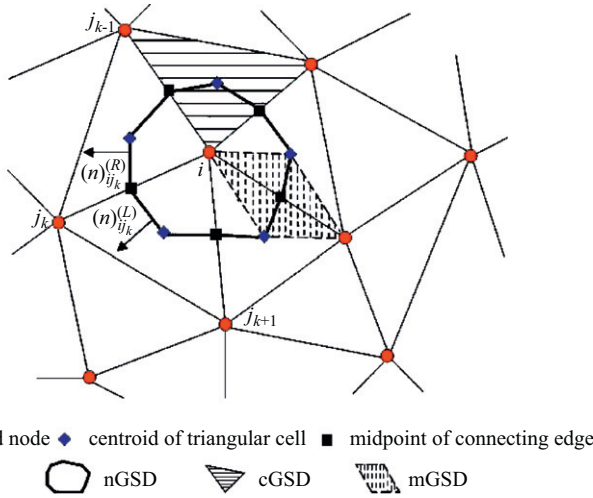


Fig. 1. Illustration of triangle cells and gradient smoothing domains defined in GSM.

of the smoothing cell Ω_i . A smooth operation to the gradient of field variable u is adopted as follows [21]:

$$\nabla^h u(\mathbf{x}_i) = \int_{\Omega_i} \nabla^h u(\mathbf{x}) \Phi(\mathbf{x} - \mathbf{x}_i) d\Omega_i \quad (10)$$

Integration by parts of Eq. (10) leads to

$$\nabla^h u(\mathbf{x}_i) = \int_{\Gamma_i} u^h(\mathbf{x}) \bar{\mathbf{n}}(\mathbf{x}) \Phi(\mathbf{x} - \mathbf{x}_i) d\Gamma - \int_{\Omega_i} u^h(\mathbf{x}) \nabla \Phi(\mathbf{x} - \mathbf{x}_i) d\Omega \quad (11)$$

where Φ is a smoothing function. $\bar{\mathbf{n}}$ denotes the unit normal vector of any one of domain faces, as shown in Fig. 1.

Consider a weighted Shepard function [22] as the smoothing function

$$\Phi(\mathbf{x} - \mathbf{x}_i) = \frac{\phi(\mathbf{x} - \mathbf{x}_i)}{\sum_{j=1}^M \phi(\mathbf{x} - \mathbf{x}_j) A_j} \quad (12)$$

where $A_i = \int_{\Omega_i} d\Omega$ is the area (or volume) of the representative domain (smoothing domain) of the i -th field node obtained from the diagram in Fig. 1. The weighted Shepard function in Eq. (12) meets the following weighted partition of unity:

$$\sum_{j=1}^M \Phi(\mathbf{x} - \mathbf{x}_j) A_j = 1 \quad (13)$$

For simplicity, a piecewise constant function ϕ is used in this work:

$$\phi(\mathbf{x} - \mathbf{x}_i) = \begin{cases} 1, & \mathbf{x} \in \Omega_i \\ 0, & \mathbf{x} \notin \Omega_i \end{cases} \quad (14)$$

Consequently the smoothing function is

$$\Phi(\mathbf{x} - \mathbf{x}_i) = \begin{cases} 1/A_i, & \mathbf{x} \in \Omega_i \\ 0, & \mathbf{x} \notin \Omega_i \end{cases} \quad (15)$$

Substituting Eq. (15) into Eq. (11), the smoothed gradient of field function u is obtained:

$$\begin{aligned} \nabla^h u(\mathbf{x}_i) &= \int_{\Gamma_i} u^h(\mathbf{x}) \bar{\mathbf{n}}(\mathbf{x}) \Phi(\mathbf{x} - \mathbf{x}_i) d\Gamma \\ &= \frac{1}{A_i} \int_{\Gamma_i} u^h(\mathbf{x}) \bar{\mathbf{n}}(\mathbf{x}) d\Gamma \end{aligned} \quad (16)$$

Note that the choice of constant Φ makes the second term on the right-hand side of Eq. (11) vanish, and the area integration becomes line integration along the edges of smoothing cell. Similarly, by successively using the smoothing procedures described in

Eqs. (10)–(16), the second-order gradients (derivatives) at the same location can be evaluated easily by differentiating Eq. (16) as

$$\nabla^2 u(\mathbf{x}_i) = \frac{1}{A_i} \int_{\Gamma_i} \nabla^h u(\mathbf{x}) \bar{\mathbf{n}}(\mathbf{x}) d\Gamma \quad (17)$$

In the current study, three types of gradient smoothing domains (GSD), which are used for approximation of spatial derivatives, are constituted on the basis of primitive unstructured triangular meshes, as shown in Fig. 1. The first is node-associated gradient smoothing domain (nGSD) that is adopted for the approximation of derivatives at any field node of interest. It is formed by connecting relevant centroids of the triangles with midpoints of the corresponding connecting edges. The second is a triangular cell itself formed by primitive mesh, which is employed for approximating derivatives (first-order) at the centroid of the cell. It is called centroid-associated gradient smoothing domain (cGSD) here. The third is named midpoint-associated gradient smoothing domain (mGSD) used for the calculation of gradients (first-order derivatives) at the midpoint of an edge of interest. The adopted favorable mGSD, as shown in Fig. 1, is formed by connecting the end-nodes of an edge of interest with the centroids of the triangles on the both sides of the edge. For approximation of the first-order derivative at any field node, only nGSD is used. For the second-order derivatives at field nodes, the values of the first-order derivative at the centroid of the triangles and midpoint of the connecting edges surrounding the node of interest are first needed. They are calculated using the cGSD and mGSD, respectively. The same nGSD is also used for the approximation of the second-order derivatives at corresponding field node. To calculate the gradients at midpoints of edges and centroids of cells with mGSD and cGSD, Eqs. (16) and (17) can also be used for approximation in the similar manner. This novel combination of use of the three types of domains provides stability and ensures the accuracy of the solution. Details will be further described in the following subsection.

2.2. Formulae for derivative approximation

We need now to evaluate the integrals along the boundaries of various types of GSDs. In this paper, two-point quadrature (trapezoidal rule) [23] is used for approximation of derivatives at nodes, midpoints and centroids. The quadrature needs the values of field variable and its gradients at the two end-nodes of each smoothing domain edge (the midpoint of the edge of interest and the centroid of the cGSD).

From Eq. (16) and using the two-point quadrature, the first-order derivatives of the field variable u are obtained

$$\begin{aligned} \frac{\partial u_i}{\partial x} &= \frac{1}{A_i} \sum_{k=1}^{n_i} \left\{ \frac{1}{2} (\Delta S_x)_{ij_k}^{(L)} [(u_m)_{ij_k} + (u_c)_{ij_k}^{(L)}] \right. \\ &\quad \left. + \frac{1}{2} (\Delta S_x)_{ij_k}^{(R)} [(u_m)_{ij_k} + (u_c)_{ij_k}^{(R)}] \right\} \end{aligned} \quad (18)$$

$$\begin{aligned} \frac{\partial u_i}{\partial y} &= \frac{1}{A_i} \sum_{k=1}^{n_i} \left\{ \frac{1}{2} (\Delta S_y)_{ij_k}^{(L)} [(u_m)_{ij_k} + (u_c)_{ij_k}^{(L)}] \right. \\ &\quad \left. + \frac{1}{2} (\Delta S_y)_{ij_k}^{(R)} [(u_m)_{ij_k} + (u_c)_{ij_k}^{(R)}] \right\} \end{aligned} \quad (19)$$

where

$$(\Delta S_x)_{ij_k}^{(L)} = \Delta S_{ij_k}^{(L)} (n_x)_{ij_k}^{(L)} \quad (20)$$

$$(\Delta S_y)_{ij_k}^{(L)} = \Delta S_{ij_k}^{(L)} (n_y)_{ij_k}^{(L)} \quad (21)$$

$$(\Delta S_x)_{ij_k}^{(R)} = \Delta S_{ij_k}^{(R)} (n_x)_{ij_k}^{(R)} \quad (22)$$

$$(\Delta S_y)_{ij_k}^{(R)} = \Delta S_{ij_k}^{(R)}(n_y)_{ij_k}^{(R)} \quad (23)$$

In above equations, ΔS_x and ΔS_y are the two components of the length of a domain edge. n_x and n_y represent the two components of the unit normal vector of a domain edge. i denotes the node of interest and j_k is the other end-node of the edge linked to node i (see Fig. 1). Superscripts (L) and (R) are pointers to the two domain faces associated with the edge of interest, ij_k . The total number of supporting nodes within the stencil of node i is denoted by n_i . These geometrical parameters are computed and stored before the intensive calculation is started. u_m and u_c denote values of field variable at midpoints of mesh-edges and centroids of triangular cells, respectively. These values are calculated by arithmetic averaging of function values at related nodes, respectively, in the fashion of

$$(u_m)_{ij_k} = \frac{u_i + u_{j_k}}{2} \quad (24)$$

$$(u_c)_{ij_k}^{(L)} = \begin{cases} (u_i + u_{j_k} + u_{j_{k+1}})/3, & k = 1, 2, \dots, n_i - 1 \\ (u_i + u_{j_{n_i}} + u_{j_1})/3, & k = n_i \end{cases} \quad (25)$$

$$(u_c)_{ij_k}^{(R)} = \begin{cases} (u_i + u_{j_k} + u_{j_{k-1}})/3, & k = 2, 3, \dots, n_i \\ (u_i + u_{j_1} + u_{j_{n_i}})/3, & k = 1 \end{cases} \quad (26)$$

Analogous to the discretization at field nodes described above, the first-order derivatives at midpoints of connecting edges ($(\nabla u_m)_{ij_k}$) and centroids of the triangles ($(\nabla u_c)_{ij_k}^{(L)}$ and $(\nabla u_c)_{ij_k}^{(R)}$) can also be approximated with the gradient smoothing technique using Eqs. (18)–(26), but based on the related mGSD and cGSD, respectively. Similarly, using Eq. (17), the second-order derivatives are given by

$$\frac{\partial^2 u_i}{\partial x^2} = \frac{1}{A_i} \sum_{k=1}^{n_i} \left\{ \begin{aligned} & \frac{1}{2}(\Delta S_x)_{ij_k}^{(L)} \left[\frac{\partial}{\partial x}(u_m)_{ij_k} + \frac{\partial}{\partial x}(u_c)_{ij_k}^{(L)} \right] \\ & + \frac{1}{2}(\Delta S_x)_{ij_k}^{(R)} \left[\frac{\partial}{\partial x}(u_m)_{ij_k} + \frac{\partial}{\partial x}(u_c)_{ij_k}^{(R)} \right] \end{aligned} \right\} \quad (27)$$

$$\frac{\partial^2 u_i}{\partial y^2} = \frac{1}{A_i} \sum_{k=1}^{n_i} \left\{ \begin{aligned} & \frac{1}{2}(\Delta S_y)_{ij_k}^{(L)} \left[\frac{\partial}{\partial y}(u_m)_{ij_k} + \frac{\partial}{\partial y}(u_c)_{ij_k}^{(L)} \right] \\ & + \frac{1}{2}(\Delta S_y)_{ij_k}^{(R)} \left[\frac{\partial}{\partial y}(u_m)_{ij_k} + \frac{\partial}{\partial y}(u_c)_{ij_k}^{(R)} \right] \end{aligned} \right\} \quad (28)$$

$$\frac{\partial^2 u_i}{\partial x \partial y} = \frac{1}{A_i} \sum_{k=1}^{n_i} \left\{ \begin{aligned} & \frac{1}{2}(\Delta S_y)_{ij_k}^{(L)} \left[\frac{\partial}{\partial x}(u_m)_{ij_k} + \frac{\partial}{\partial x}(u_c)_{ij_k}^{(L)} \right] \\ & + \frac{1}{2}(\Delta S_y)_{ij_k}^{(R)} \left[\frac{\partial}{\partial x}(u_m)_{ij_k} + \frac{\partial}{\partial x}(u_c)_{ij_k}^{(R)} \right] \end{aligned} \right\} \quad (29)$$

All the first-order derivatives used in Eqs. (27)–(29) are approximated as previously described.

2.3. Analyses of discretization stencil

Before conducting intensive numerical investigations, careful theoretical studies of the stencils of supporting nodes for the node where derivatives are approximated using GSM are carried out. The objective for stencil analyses is to validate if the GSM satisfies the basic principles of numerical discretization. The stencils for approximating the gradients ($\partial u_i/\partial x, \partial u_i/\partial y$) and Laplace operator using both uniform Cartesian and equilateral triangular meshes are focused in this section.

In the stencil analyses, the following five basic rules are considered to assess the quality of a stencil resulting from a discretization scheme: (a) consistency at each domain face; (b) positivity of coefficients of influence; (c) negative-slope linearization of the source term; (d) sum of the neighbor coefficients, and (e) the compactness

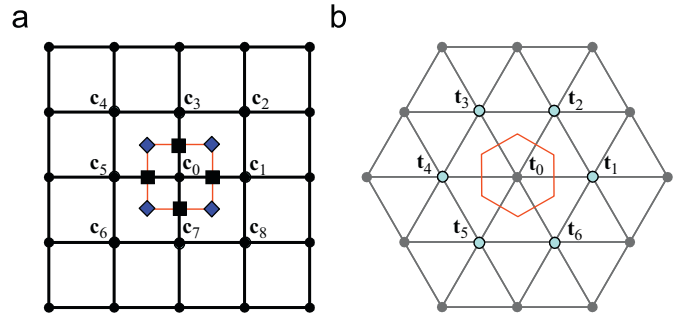


Fig. 2. Stencils for approximated gradients discretized on (a) uniform Cartesian mesh; (b) equilateral triangular mesh.

of the stencil. The first four rules are summarized by Patankar [24] with consideration of solutions with physically realistic behavior and overall balance. To satisfy Rule (a), it requires that the same expression of approximation must be used on the interface of two adjacent GSDs, so that when the gradient smoothing technique is applied to the GSDs, the local conservation of quantities is automatically ensured and so for the global conservation. Rule (b) requires that the coefficient for the node of interest and the coefficients of influence must be positive, once the discretization equation is written in the form of $a_{ii}u_i = \sum_{k=1}^{n_i} a_{ij_k} u_{j_k} + b_i$. Rule (c) relates to the treatment of the source terms. As addressed by Patankar [24], it is essential to keep the slope of linearization to be negative, since a positive slope can lead to computational instabilities and physically unrealistic solutions. Rule (d) tells $a_{ii} = \sum_{k=1}^{n_i} a_{ij_k}$. Barth [25] has proposed a few lemmas to address the necessity of positivity of coefficients to satisfy a discrete maximum principle that is a key tool in the design and analysis of numerical schemes suitable for non-oscillatory discontinuity (for example, shock). At steady state, non-negativity of the coefficients becomes sufficient to satisfy a discrete maximum principle that can be applied successively to obtain global maximum principle and stable results. His statements reiterate the importance of Rule (b) as mentioned by Patankar [24]. In addition, as commented by Barth [25], the very first layer of nodes surrounding the node of interest should be included in its stencil. Moreover, as the stencil becomes larger, not only the computational cost increases, but eventually the accuracy decreases as less valid data from further away is brought into approximation. Thus, for the concerns about numerical accuracy and efficiency, Rule (e) on the compactness of the stencil is adopted as additional factor for the assessment of discretization scheme of GSM.

Fig. 2 demonstrates the stencils for approximated gradients ($\partial u_i/\partial x, \partial u_i/\partial y$) and ($\partial^2 u_i/\partial x^2 + \partial^2 u_i/\partial y^2$). For the first-order derivatives ($\partial u_i/\partial x, \partial u_i/\partial y$), the stencil is $\mathbf{c}_1 = (\frac{3}{8}, 0)$, $\mathbf{c}_2 = (\frac{1}{16}, \frac{1}{16})$, $\mathbf{c}_3 = (0, \frac{3}{8})$, $\mathbf{c}_4 = (-\frac{1}{16}, \frac{1}{16})$, $\mathbf{c}_5 = (-\frac{3}{8}, 0)$, $\mathbf{c}_6 = (-\frac{1}{16}, -\frac{1}{16})$, $\mathbf{c}_7 = (0, -\frac{3}{8})$, $\mathbf{c}_8 = (\frac{1}{16}, -\frac{1}{16})$ and $\mathbf{c}_0 = (0, 0)$ for uniform Cartesian mesh. It is observed that the stencil is identical to that of six-point based central-differencing scheme in the FDM. This finding confirms that when uniform Cartesian meshes are used, the GSM is identical to the FDM. The GSM, however, works for irregular meshes. The stencil on equilateral triangular mesh is $\mathbf{t}_1 = (\frac{1}{3}, 0)$, $\mathbf{t}_2 = (\frac{1}{6}, \frac{\sqrt{3}}{6})$, $\mathbf{t}_3 = (-\frac{1}{6}, \frac{\sqrt{3}}{6})$, $\mathbf{t}_4 = (-\frac{1}{3}, 0)$, $\mathbf{t}_5 = (-\frac{1}{6}, -\frac{\sqrt{3}}{6})$, $\mathbf{t}_6 = (\frac{1}{6}, -\frac{\sqrt{3}}{6})$ and $\mathbf{t}_0 = (0, 0)$. This stencil is identical to that of interpolation method using six surrounding nodes. Note that for irregular triangular meshes, the interpolation method will fail as addressed by Liu [1], but our GSM still performs well, as will be demonstrated in the section on numerical examples. This is due to the crucial stability provided by the smoothing operation.

Table 1
Truncation errors in the approximation of first-order derivatives in GSM

Type of mesh	Truncation error
Uniform Cartesian	$O_x(h^2) = -h^2 \left(\frac{5}{24} \frac{\partial^3 u_{ij}}{\partial x^3} + \frac{1}{2} \frac{\partial^3 u_{ij}}{\partial x \partial y^2} \right) + O(h^3)$
	$O_y(h^2) = -h^2 \left(\frac{5}{24} \frac{\partial^3 u_{ij}}{\partial y^3} + \frac{1}{2} \frac{\partial^3 u_{ij}}{\partial x^2 \partial y} \right) + O(h^3)$
Equilateral triangular	$O_x(h^2) = -h^2 \left(\frac{1}{24} \frac{\partial^3 u_i}{\partial x^3} + \frac{1}{8} \frac{\partial^3 u_i}{\partial x \partial y^2} \right) + O(h^3)$
	$O_y(h^2) = -h^2 \left(\frac{1}{24} \frac{\partial^3 u_i}{\partial y^3} + \frac{1}{8} \frac{\partial^3 u_i}{\partial x^2 \partial y} \right) + O(h^3)$

Table 2
Truncation errors in the approximation of Laplace operator in GSM

Type of mesh	Truncation error
Uniform Cartesian	$O(h^2) = -\frac{h^2}{12} \left(\frac{\partial^4 u_{ij}}{\partial x^4} + 3 \frac{\partial^4 u_{ij}}{\partial x^2 \partial y^2} + \frac{\partial^4 u_{ij}}{\partial y^4} \right) + O(h^3)$
Equilateral triangular	$O(h^2) = -\frac{h^2}{16} \left(\frac{\partial^4 u_i}{\partial x^4} + 2 \frac{\partial^4 u_i}{\partial x^2 \partial y^2} + \frac{\partial^4 u_i}{\partial y^4} \right) + O(h^3)$

Compact stencils for approximated Laplace operator ($\partial^2 u_i / \partial x^2 + \partial^2 u_i / \partial y^2$) with quite favorable weighting coefficients are obtained on both uniform Cartesian ($\mathbf{c}_1 = \mathbf{c}_3 = \mathbf{c}_5 = \mathbf{c}_7 = \frac{1}{2}, \mathbf{c}_2 = \mathbf{c}_4 = \mathbf{c}_6 = \mathbf{c}_8 = \frac{1}{4}, \mathbf{c}_0 = 3$) and equilateral triangular ($\mathbf{c}_1 = \mathbf{c}_2 = \mathbf{c}_3 = \mathbf{c}_4 = \mathbf{c}_5 = \mathbf{c}_6 = \frac{2}{3}, \mathbf{c}_0 = 4$) meshes, as shown in Fig. 2. Truncation errors in the approximation of first- and second-order derivatives with the present GSM are also derived using Taylor series expansion based on uniform Cartesian mesh and equilateral triangular mesh, respectively, as summarized in Tables 1 and 2. It is clear that GSM is of second-order accuracy. This is further confirmed when the GSM is used to approximate solutions to numerical examples in the following section.

3. Adaptive scheme

A good error indicator is of great importance in the adaptive analysis. In this paper, a robust error indicator based on residual of the governing equations [26] is adopted. The residual based error indicator provides a good measurement for the quality of the local approximation and the global accuracy of the solution. The details of the error indicator and refinement procedures are given as follows.

3.1. Error indicator

In this adaptive scheme, the same set of triangular cells used for GSDs is used. The error indicator for a triangular cell is computed by evaluating the residual of the strong form governing equations at the centroid of the triangular cell, as shown in Fig. 1. In this work, we use two types of error indicators: local and global error indicators. The local indicator is used to determine the cells that need to be refined, and the global error indicator is used to control the iterations of refinement. The local error indicator is defined as

$$\eta_j = \int \|\mathbf{L}\mathbf{u} - \mathbf{f}\|_{L_2} d\Omega \approx \frac{1}{3} A_j \|Lu_j - f_j\|_{L_2} \quad (30)$$

where A_j is the area of the j -th cell, and $\|Lu_j - f_j\|_{L_2}$ is the L_2 norm of the residual for the governing equation evaluated at the center of corresponding cell by simple interpolation using the nodal values of the displacements.

With the above definition of the local error indicator, the global error indicator is estimated using the global residual norm that can

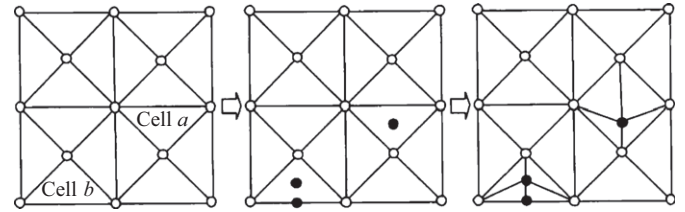


Fig. 3. Illustration of the refinement procedure: (○) old node; (●) new node.

be easily obtained as

$$\eta_g = \sqrt{\int (\|\mathbf{L}\mathbf{u} - \mathbf{f}\|_{L_2})^2 d\Omega} \approx \sqrt{\sum_{j=1}^{n_c} \left[\frac{1}{3} A_j (Lu_j - f_j) \right]^2} \quad (31)$$

where n_c is the total number of the triangular cells.

3.2. Refinement procedure and stopping criterion

The refinement criterion for the j -th cell in our adaptive scheme is that when

$$\eta_j \geq \kappa_1 \max_{1 \leq i \leq n_c} (\eta_i) \quad (32)$$

cell j is refined, where κ_1 is a local refinement coefficient defined by the analyst. Eq. (32) simply leads that a certain percentage of cells that have maximum errors are refined. In advance, the triangular cells are classified into two groups: interior cells and edge cells. An interior cell is a cell that has no edge on the boundaries of the problem domain, and an edge cell is a cell which has at least one edge on the boundaries. For example, cell a and cell b are interior and edge cells, respectively, as shown in Fig. 3. Then if this interior cell needs to be refined, a new node will be added at the centroid of the triangle; for an edge cell, two new nodes will be added at the centroid and the midpoint of the edge which is on the boundaries (see Fig. 3). Finally, the formation of the new mesh will be performed using the Delaunay technique based on the new nodes, as sketched in Fig. 3.

The estimated global residual norm defined in Eq. (31) is used as an indicator for termination criterion of the adaptive process. The stopping criterion is that when

$$\eta_g \leq \kappa_g \eta_{mg} \quad (33)$$

is met the adaptive process will be terminated, where κ_g is the global residual tolerant coefficient and η_{mg} is the allowable maximum value of global residual error throughout the adaptive process.

4. Numerical examples

In the numerical studies, a norm of the true error for field variable u is defined as

$$e_u = \sqrt{\frac{\sum (u^{\text{numerical}} - u^{\text{analytical}})^2}{\sum (u^{\text{analytical}})^2}} \quad (34)$$

where $u^{\text{analytical}}$ is the analytical solution and $u^{\text{numerical}}$, the numerical solution.

4.1. Patch test

In the first example, both standard patch test with maximum (full) essential boundaries called essential-patch-test here and a

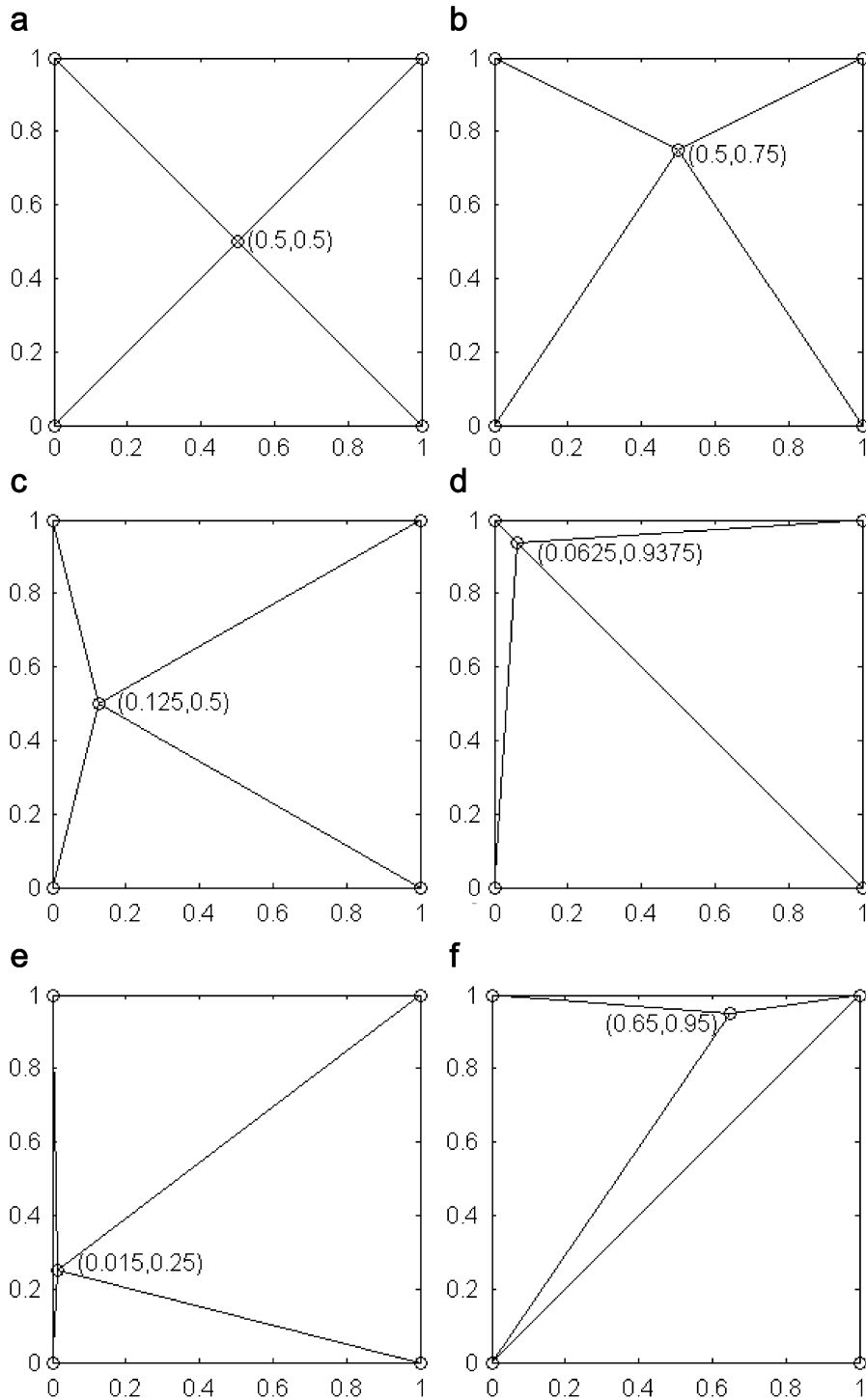


Fig. 4. Patches of five nodes in the essential-patch-test.

patch test with maximum natural boundaries called natural-patch-test here are conducted using the present GSM. For essential-patch-test, six different patches of a solid are first examined as shown in Fig. 4. All patches have only five field nodes: four corner nodes and one inner node whose location varies inside the domain. The dimension of the patch is 1×1 , and the material properties are taken as Young's modulus $E = 1.0$ and Poisson's ratio $\nu = 0.25$. The displacements are prescribed on the outside boundaries using a linear

function of x and y :

$$u_x = x + y \quad \text{and} \quad u_y = x - y \tag{35}$$

To satisfy the patch test, it requires that the displacements of any interior nodes should be given by the same linear functions in the patch test. As given in Table 3, all six patches have passed the standard patch test to machine accuracy. It is found that all patches have

Table 3
True error norms of displacements for essential-patch-test

Patch	Error norm of u_x	Error norm of u_y
Patch a	6.2944E-16	6.3624E-16
Patch b	1.6149E-16	2.7057E-16
Patch c	2.1959E-16	3.4147E-16
Patch d	1.6785E-16	5.3408E-16
Patch e	1.8025E-16	3.2913E-16
Patch f	9.8661E-16	2.3039E-16

Table 4
True error norms of displacements for natural-patch-test

Patch	Error norm of u_x	Error norm of u_y
Regular nodes	1.1019E-14	7.9795E-14
Irregular nodes	8.5544E-14	2.7266E-12

It is observed that the two patches of both regular and irregular node distributions pass the higher-order patch test to machine accuracy, as given in Table 4. This shows again that the GSM has excellent stability.

It is known that the essential-patch-test is more critical to methods based on global weak-forms, and the natural-patch-test is, on the other hand, more critical to methods based on strong forms [2]. Our GSM passes both, which proves numerically that GSM is capable of producing linear fields regardless of types of boundary condition, and hence the GSM solution will converge to any high order continuous fields. More details of conducting the patch tests can be found in Refs. [1,2,5].

4.2. Poisson's equation with a sharp peak

In the second example, we test further the stability, accuracy, and the peak capturing ability of our GSM using adaptive scheme, and study a Poisson's problem whose solution has a very sharp peak. Such a Poisson's equation is defined as

$$\nabla^2 u = [-400 + (200x - 100)^2 + (200y - 100)^2] \times e^{-100(x-(1/2))^2 - 100(y-(1/2))^2} \tag{37}$$

in the domain of $\Omega: [0, 1] \times [0, 1]$, with Neumann boundary conditions,

$$\frac{\partial u}{\partial n} = 0 \text{ along } \Gamma_T: x = 0 \text{ and } y = 0 \tag{38}$$

and Dirichlet boundary conditions,

$$u = 0 \text{ along } \Gamma_U: x = 1 \text{ and } y = 1 \tag{39}$$

The analytical solution for this problem is given as

$$u = e^{-100(x-(1/2))^2 - 100(y-(1/2))^2} \tag{40}$$

Because the analytical solution is available for this problem, the true error in the numerical solution of GSM can be examined.

The Poisson's equation is first solved using our GSM with the six regular distributions of 11×11 , 16×16 , 21×21 , 30×30 , 46×46 and 61×61 (=3721) field nodes. Four selected node distributions (regular left triangular meshes) are shown in Fig. 6. The overall true error norm of the field variable u is reduced from 33.54% to 0.51% as the mesh is refined uniformly, as given in Table 5. This shows that the present GSM is very stable and accurate. The Poisson's equation is now studied again using our GSM, but with adaptive analysis. The initial mesh has 121 regularly distributed nodes (see Fig. 6). The adaptive procedure ends up at fifth iteration step with 1107 irregularly distributed nodes in the problem domain. The local pre-defined refinement coefficient is $\kappa_l = 0.05$ and the global residual tolerant coefficient is set as $\kappa_g = 0.1$. Due to the presence of sharp peak, most of the nodes are inserted automatically into the high gradient region as shown in Fig. 7. This demonstrates the fact that our GSM is capable of capturing the 'peak'. From Fig. 8, one can observe that the estimated global residual is reduced steadily. This shows the excellent stability of the present GSM, even for extremely irregularly distributed nodes. While estimated global residual norm is reduced in the adaptive process, the true error norm of field function u is reduced from 33.54% to 0.56% as given in Table 6. Compared with the uniform refinement with 3721 regular nodes, the similar

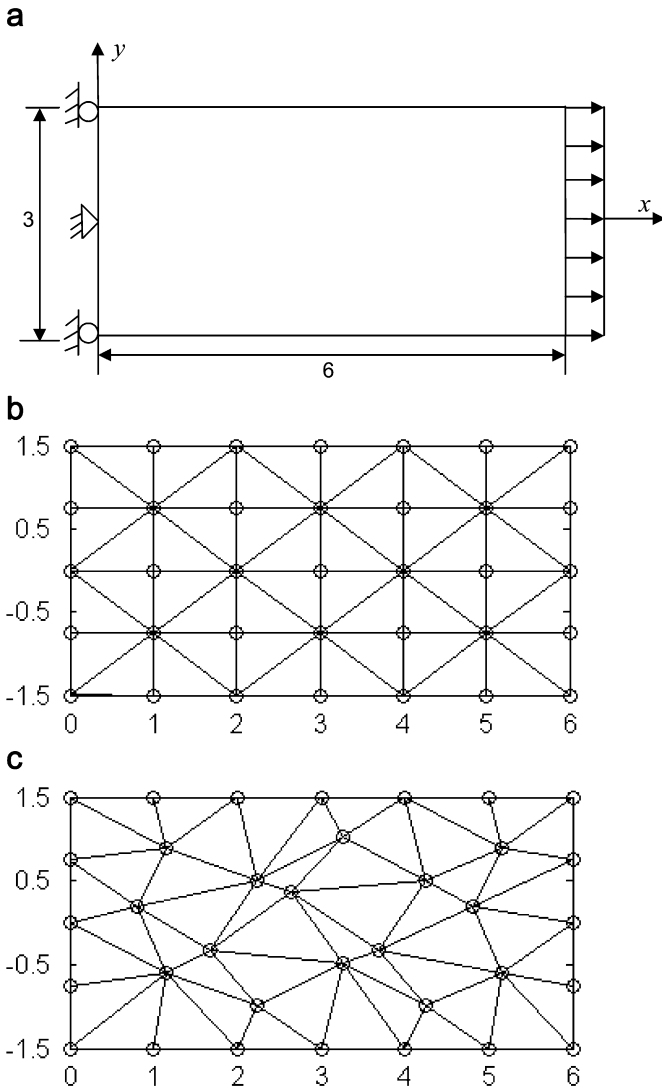


Fig. 5. (a) Patches for the natural-patch-test: a uniform axial traction along the right end of the patch; (b) patch with 35 regular nodes; (c) patch with 35 irregular nodes.

the same level of accuracy regardless of the irregularity of the cells in the patches. This demonstrates the good stability of the proposed GSM.

In natural-patch-test, two different patches are subjected to a uniform axial traction of unit intensity along the right end of the cantilever beam, as shown in Fig. 5. There are 35 nodes regularly distributed in the first patch (see Fig. 5(b)) and irregularly distributed in the second patch (see Fig. 5(c)). The dimension of the cantilever beam is 3.0×6.0 . The material properties are also taken as $E = 1.0$ and $\nu = 0.25$. The exact solutions of the displacements for this problem are

$$u_x = x \text{ and } u_y = -y/4 \tag{36}$$

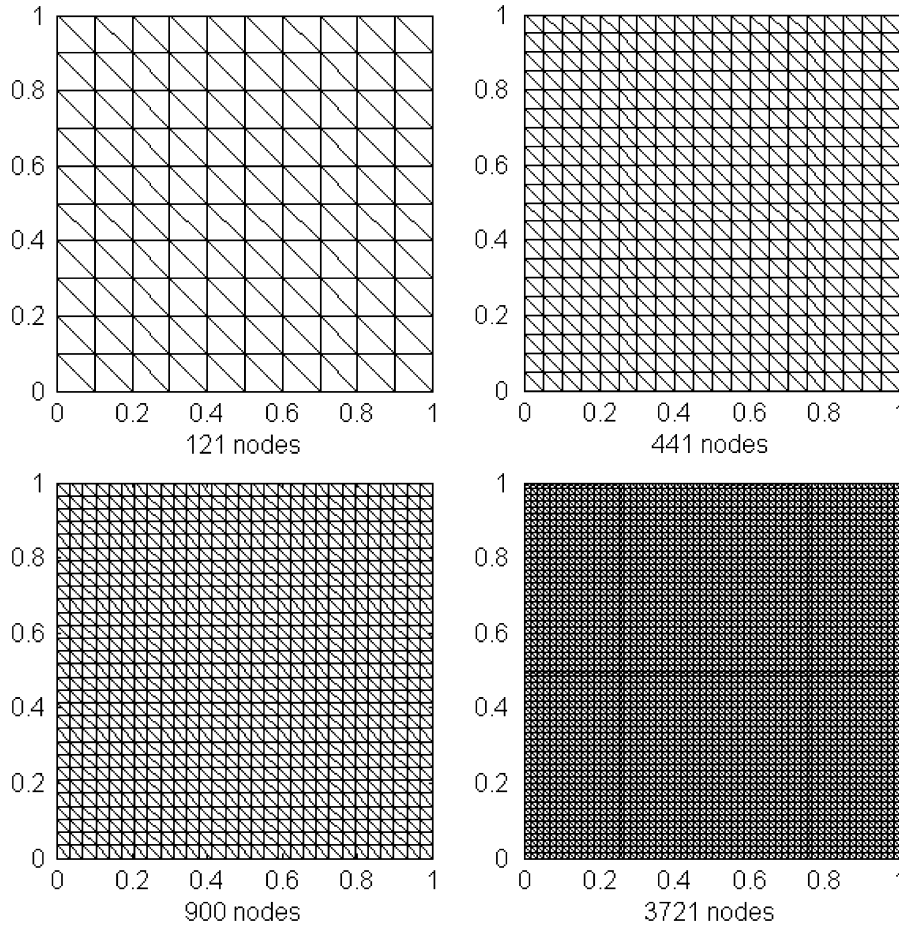


Fig. 6. Node distributions of uniform refinement for Poisson's equation with a sharp peak at the center.

Table 5 True error norms of uniform refinement for Poisson's equation with a sharp peak

No. of field nodes	121	256	441	900	2116	3721
Error norm (%)	33.54	9.02	4.84	2.22	0.91	0.51

accuracy can be obtained using the adaptive refinement with only 1107 nodes. The comparison of convergence rate (R) between uniform and adaptive refinements is plotted in Fig. 9, where h is the averaged cell size. The convergence rate for the uniform refinement is found to be about 2.07 that conforms the theoretical prediction of 2.0 as given in Table 1. The adaptive refinement using GSM achieves a convergence rate of about 3.14 for field function u which is much higher compared with the uniform refinement.

The GSM solutions for field function u along the line $y = 0.5$ at the first and fifth (final) steps are plotted with analytical solution in Fig. 10. It is clear that this adaptive scheme is effective to improve in an automatically manner the accuracy of the solution for field function u . The three-dimensional plots of the approximated field function and its derivatives at the final step are provided in Fig. 11. It shows not only the approximated field function but also field function derivatives are in very good agreement with the analytical solutions in Eq. (40).

4.3. Infinite plate with a circular hole

This numerical example is a stress analysis of an infinite plate with a central circular hole subjected to a unidirectional tensile load $p = 1.0$ in the x -direction. A plane strain problem is considered. The

problem has stress concentration near the hole, and hence is a good test of our adaptive GSM for stress concentration capturing. Due to the symmetry, only the upper right quadrant of the plate is modeled, as shown in Fig. 12. The geometry and material parameters used are $a = 1, b = 5$, Young's modulus $E = 1.0 \times 10^3$ and Poisson's ratio $\nu = 0.3$.

The governing equations of this problem are given by Eqs. (1)–(3), which are also used for the following numerical investigations. Symmetric boundary conditions are imposed on the left and bottom edges, and the inner boundary of the hole is traction free. The corresponding exact solutions for the stresses in the plate are given in the polar coordinate [27]:

$$\sigma_{xx} = 1 - \frac{a^2}{r^2} \left(\frac{3}{2} \cos 2\theta + \cos 4\theta \right) + \frac{3}{2} \frac{a^4}{r^4} \cos 4\theta \tag{41}$$

$$\sigma_{xy} = -\frac{a^2}{r^2} \left(\frac{1}{2} \sin 2\theta + \sin 4\theta \right) + \frac{3}{2} \frac{a^4}{r^4} \sin 4\theta \tag{42}$$

$$\sigma_{yy} = -\frac{a^2}{r^2} \left(\frac{1}{2} \cos 2\theta - \cos 4\theta \right) - \frac{3}{2} \frac{a^4}{r^4} \cos 4\theta \tag{43}$$

where (r, θ) are the polar coordinates and θ is measured counter-clockwise from the positive x -axis. The traction boundary conditions given by the exact solutions (41)–(43) are imposed on the right ($x = 5$) and top ($y = 5$) edges.

Because the analytical solution is also available for this problem, the true error in the numerical solution of GSM can be examined. Using the present GSM, we start this benchmark problem from approximately uniform refinement with 39, 98, 199, 403, 826 and 1513 field nodes. Also, four selected node distributions are shown in

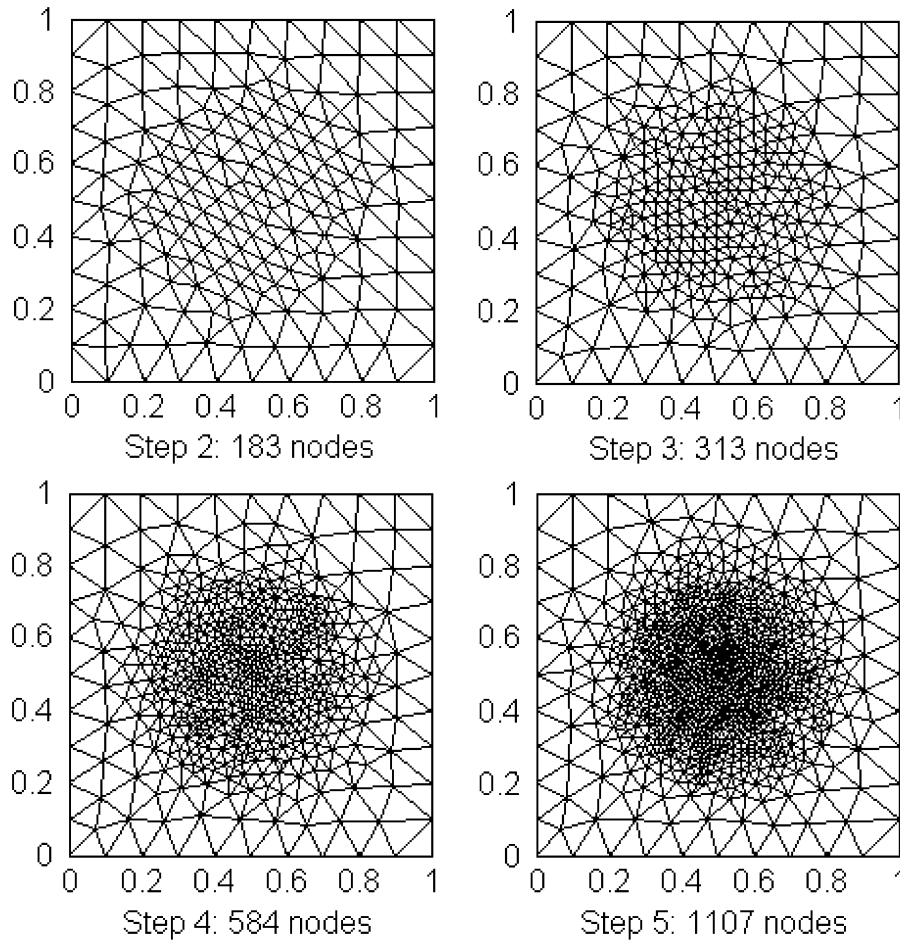


Fig. 7. Adaptive node distributions from the second to fifth step for solving Poisson's equation.

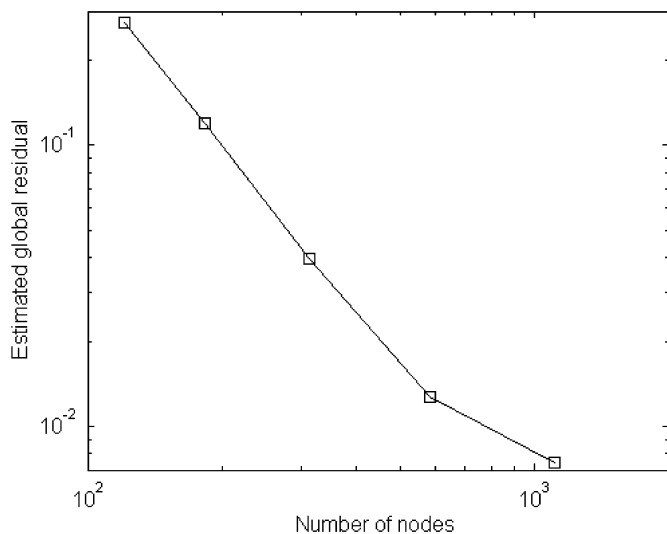


Fig. 8. Estimated global residual at each adaptive step for solving Poisson's equation.

Table 6 True error norms of adaptive refinement for Poisson's equation with a sharp peak

	Step				
	1	2	3	4	5
No. of field nodes	121	183	313	584	1107
Error norm (%)	33.54	8.66	3.09	1.10	0.56

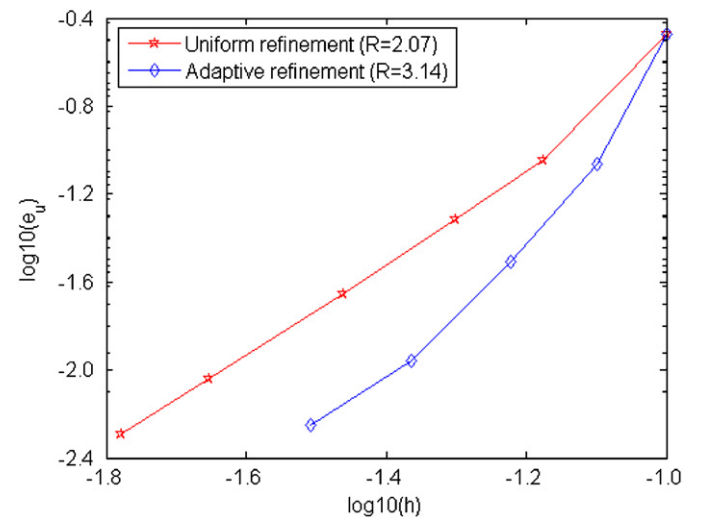


Fig. 9. Comparison of error and convergence rate between uniform and adaptive refinements for solving Poisson's equation with a sharp peak.

Fig. 13. As given in Table 7, the true error norm of the displacement u_x is steadily reduced from 90.12% to 0.98%. This shows again that the GSM has very good stability and accuracy. The adaptive analysis using GSM starts with 39 nodes 'evenly' distributed in the quarter model (see Fig. 13). The local refinement coefficient is set as $\kappa_l=0.05$ and the global residual tolerant coefficient is predefined as $\kappa_g=0.05$.

As shown in Fig. 14, the adaptive analysis ends at the sixth step with 567 nodes irregularly distributed in the problem domain.

The estimated global residual at each adaptive step is plotted in Fig. 15. One can observe that the global residual norm is gradually reduced at each adaptive step. It demonstrates again the excellent stability of the GSM even when irregular nodes are used.

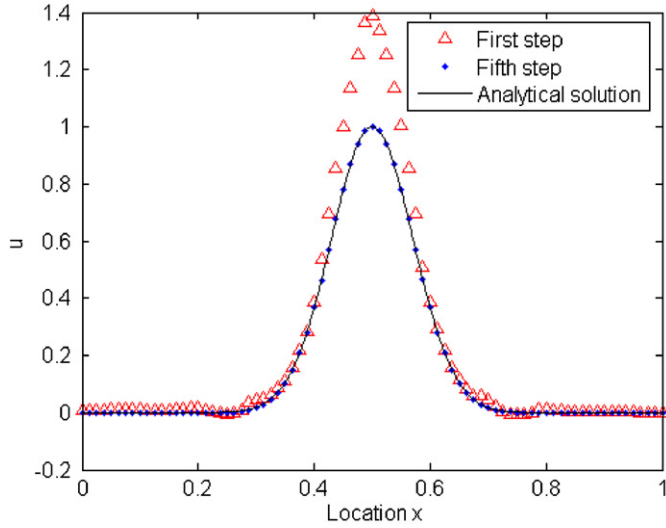


Fig. 10. Approximated values of field function u along the line $y=0.5$ at the first and fifth steps.

The error norms of the displacement u_x are given in Table 8. Compared Table 8 with Table 7, the GSM with uniform refinement can

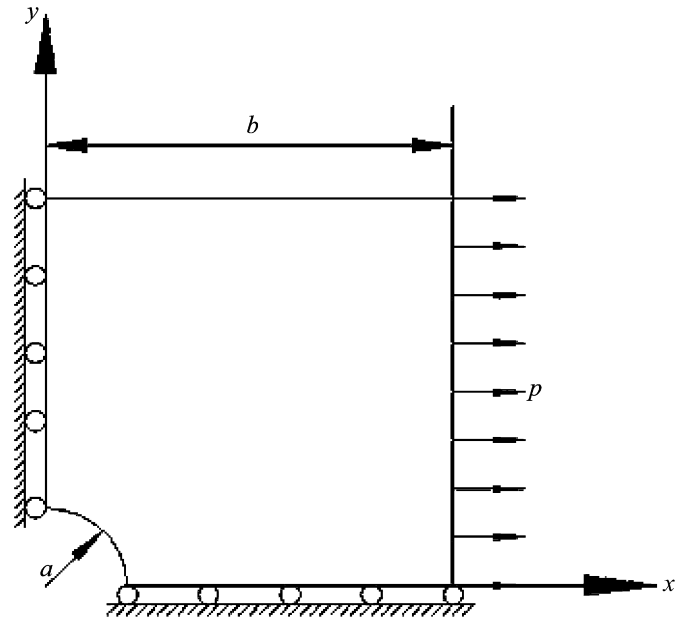


Fig. 12. Quarter model of the infinite plate with a circular hole subjected to a unidirectional tensile load.

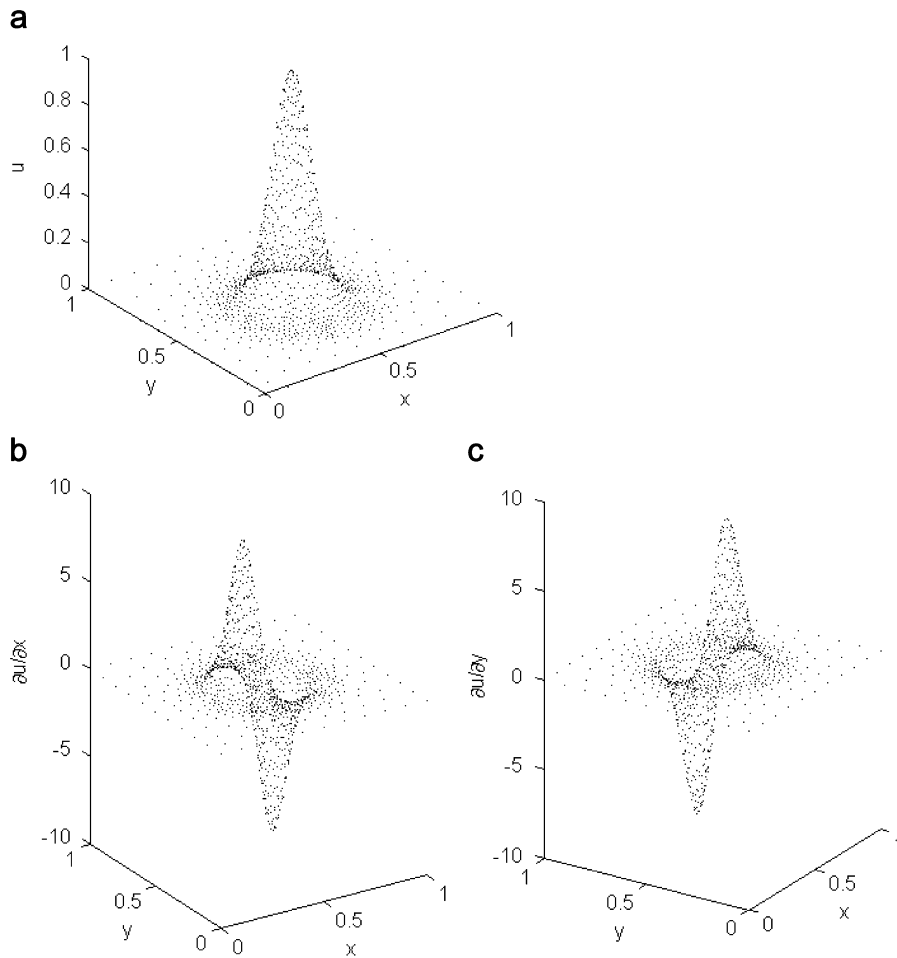


Fig. 11. The three-dimensional plots of adaptive GSM solutions for Poisson's equation with a sharp peak at the final adaptive step: (a) u ; (b) $\partial u/\partial x$; (c) $\partial u/\partial y$.

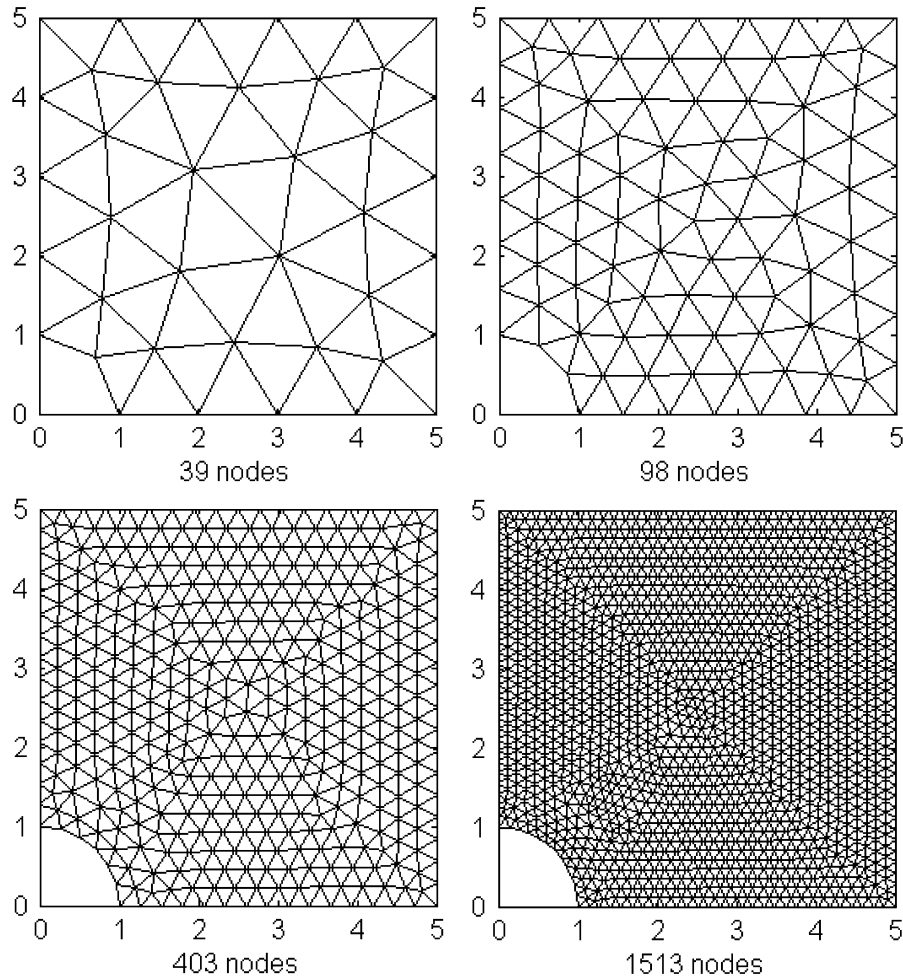


Fig. 13. Node distributions of uniform refinement for quarter model of infinite plate: from 39 to 1513 nodes.

Table 7
True error norms of uniform refinement for infinite plate with a circular hole

No. of field nodes	39	98	199	403	826	1513
Error norm of u_x (%)	90.12	39.68	6.59	1.67	1.12	0.98

only bring the true error norm down to 0.98% with 1513 nodes while the error can be brought down to 0.48% using the GSM for adaptive refinement with 567 nodes. As the node increases further, the error norm reduces very slowly for the 'uniform' refinement case due to the stress concentration that is not uniform but only near the hole. However, for the GSM with the adaptive refinement, the error norm is reduced at a steady rate, because of its ability to capture the stress concentration. For validation purpose, the distributions of normal stress σ_{xx} along the line $x=0$ at the third and sixth steps are plotted in Fig. 16. It is very clear that the accuracy of both displacement and stress has been improved a lot through the effective adaptive scheme using the GSM for the stress concentration problem.

4.4. Short cantilever plate

In this example, the GSM is used for the stress analysis of a short cantilever plate subjected to a uniformly distributed pressure on the top, as shown in Fig. 17. The problem is solved as a plain strain case with material properties $E = 1.0$, $\nu = 0.3$ and loading $p = 1.0$. This problem has stress singularity near the two left corners, and

hence is very good for testing our adaptive GSM for stress singularity capturing. As analyzed in the work of Johnson and Hansbo [28] and Steeb et al. [29], the exact solution of energy norm $\|\mathbf{u}\|$ is defined as

$$\|\mathbf{u}\| = \left(\int_{\Omega} \boldsymbol{\sigma}^T \boldsymbol{\epsilon} \, d\Omega \right)^{1/2} \tag{44}$$

and found to be 1.379745. Since the analytical solution for the displacements is not known, a reference solution is obtained using a very fine mesh of 58 060 degrees of freedom. The calculated energy norm $\|\mathbf{u}_h\|$ using this very fine mesh is 1.3794663, which is almost the exact energy of 1.379745. The calculated value of displacement in y -direction at the tip node $A(1, 0)$ is -2.875323 . We assume this value as reference 'exact' solution.

The uniform refinement for this example uses six regular meshes with 73, 214, 488, 755, 1376 and 2498 evenly distributed nodes. Four such distributions of nodes are shown in Fig. 18. The GSM solutions of displacement $u_y(A)$, energy norm and their error norms are presented in Table 9. In this paper, the relative error in energy norm is defined as

$$e_e = \left| \frac{\|\mathbf{u}_h\| - \|\mathbf{u}\|}{\|\mathbf{u}\|} \right| \tag{45}$$

As the uniform refinement advances, both the displacement $u_y(1, 0)$ and energy norm approach the 'exact' (reference) solutions gradually.

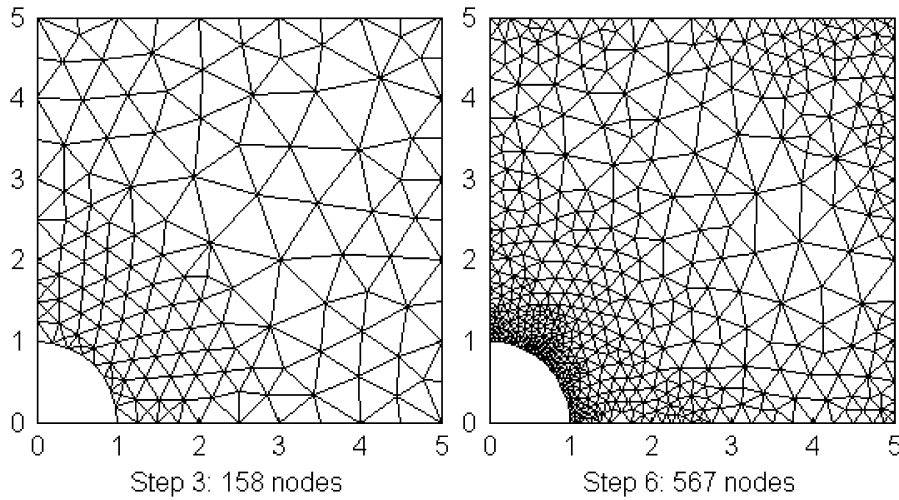


Fig. 14. Node distributions of adaptive refinement at the third and sixth steps for the quarter model of infinite plate with a circular hole.

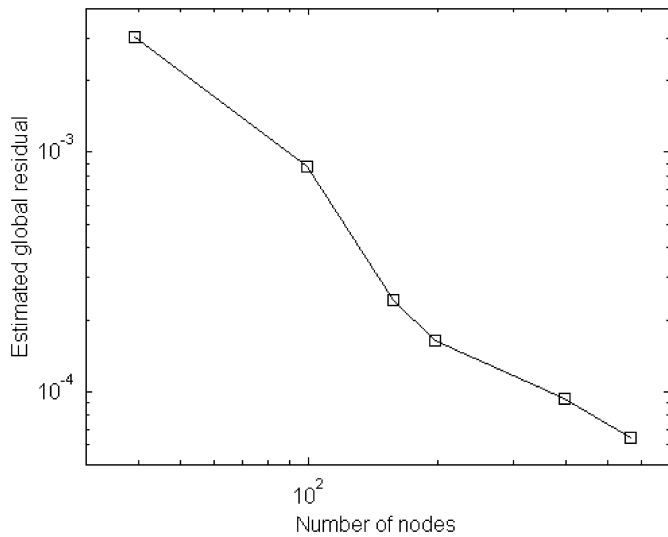


Fig. 15. Estimated global residual at each adaptive step for the infinite plate.

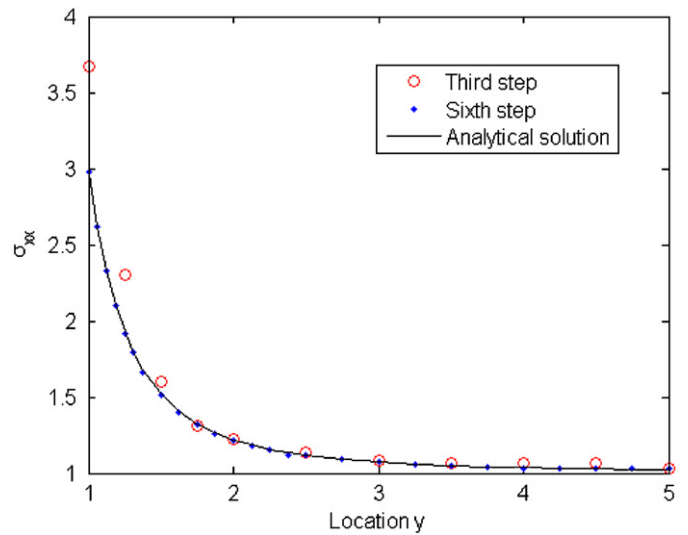


Fig. 16. Normal stress σ_{xx} along $x=0$ at the third and sixth steps.

Table 8 True error norms of adaptive refinement for infinite plate with a circular hole

	Step					
	1	2	3	4	5	6
No. of field nodes	39	99	158	197	395	567
Error norm of u_x (%)	90.12	8.88	3.01	2.18	0.78	0.48

The adaptive refinement starts with the same coarse mesh of 73 field nodes as shown in Fig. 18. The local refinement coefficient is predetermined as $\kappa_l=0.05$ and the global residual tolerant coefficient is set as $\kappa_g=0.05$. As shown in Fig. 19, the adaptive analysis ends at the sixth step with 1889 nodes distributed irregularly in the whole plate domain. Due to the stress concentration in this problem, more nodes are added into the two corner areas at the left side of the plate (see Fig. 19). It can be observed from Fig. 20 that the estimated global residual is monotonically reduced as nodes increase. Table 10 presents displacement at point A, energy and their error norms for each adaptive step. Compared with the results of uniform refinement, the GSM with adaptive scheme is clearly more effective. It leads to a

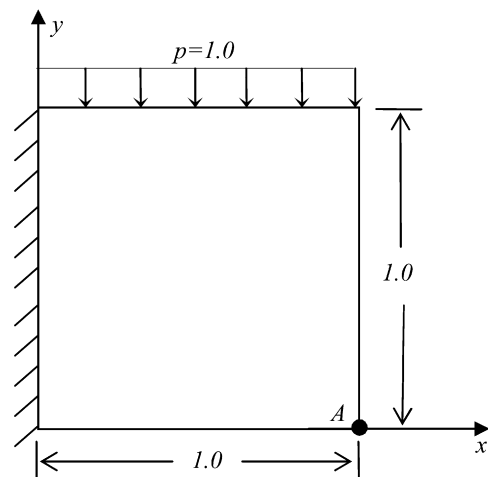


Fig. 17. A short cantilever plate subjected to a uniformly distributed pressure on the top.

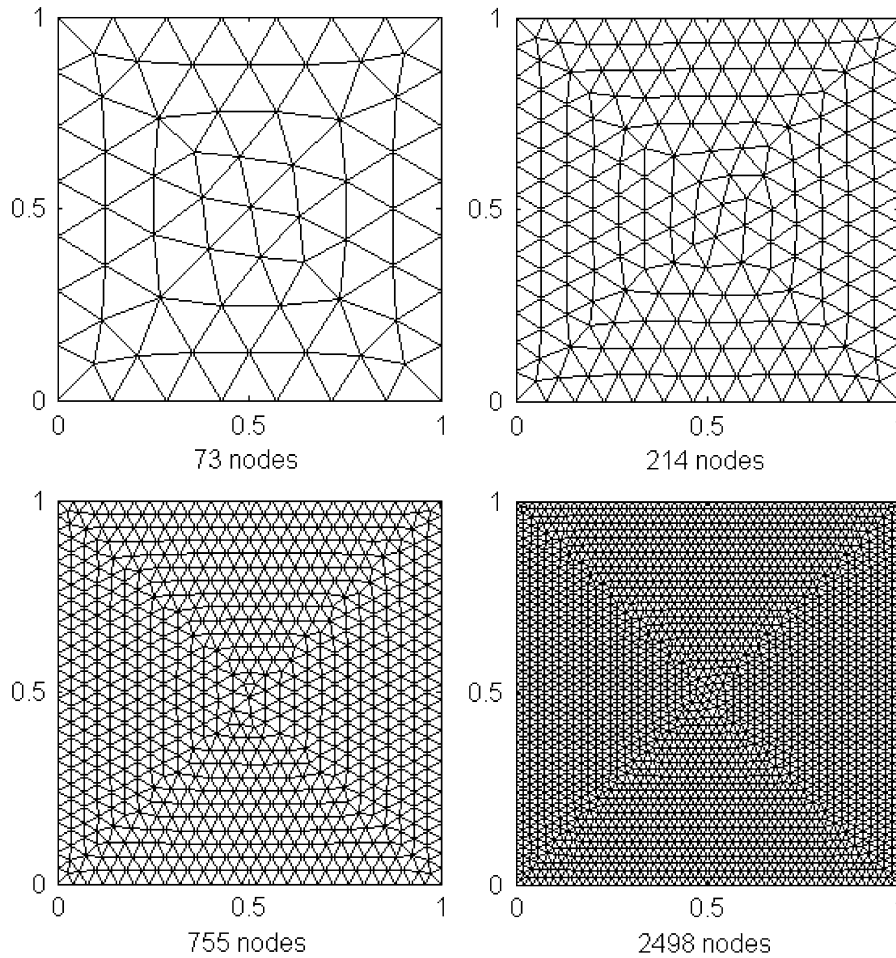


Fig. 18. Node distributions of 'uniform' refinement for short cantilever plate.

Table 9
Error norms of uniform refinement for short cantilever plate

No. of field nodes	73	214	488	755	1376	2498
<i>u_y</i> (1,0)						
GSM						
Value	-2.5170	-2.6748	-2.7397	-2.7592	-2.7901	-2.8094
Error norm (%)	12.46	6.98	4.72	4.04	2.96	2.29
FEM						
Value	-2.7581	-2.8277	-2.8503	-2.8575	-2.8643	-2.8685
Error norm (%)	4.08	1.65	0.87	0.62	0.38	0.24
Energy						
GSM						
Value	1.2867	1.3344	1.3521	1.3566	1.3642	1.3683
Error norm (%)	6.74	3.29	2.00	1.68	1.13	0.83
FEM						
Value	1.3492	1.3668	1.3727	1.3746	1.3764	1.3776
Error norm (%)	2.21	0.94	0.51	0.37	0.24	0.16

very fine accuracy using much less nodes, as shown in Figs. 21 and 22. The comparison of convergence rate in energy norm between uniform and adaptive refinements is demonstrated in Fig. 23. The convergence rate obtained using the adaptive scheme with GSM is much higher than that of uniform refinement.

For comparison purpose, we now study the present problem using linear FEM with both uniform and adaptive models with the same set of initial nodes as that used in the GSM. The adaptive procedure used in the FEM is also the same as that used in adaptive

GSM with the same tolerant coefficients. Table 9 also presents the FEM solutions of displacement $u_y(A)$, energy norm and their error norms for the uniform refinement. Table 11 presents displacement at point A, energy and their error norms for each adaptive step. The comparisons of GSM and FEM with both uniform and adaptive refinements are plotted in Figs. 21 and 22. The energy errors of the numerical results calculated using Eq. (45) are plotted in Fig. 23 with respect to h . Here, h is taken as the average nodal spacing for different nodal configurations. The results show that the adaptive models for both GSM and FEM have obtained higher convergence rate than uniform refinements. This demonstrates the effectiveness of the present adaptive procedure. Second, compared with FEM, the GSM achieves much higher convergence rate for adaptive refinement.

Fig. 24 presents the comparison of condition numbers of the coefficient matrix for both uniform and adaptive refinements. For uniform refinement, GSM has almost the same condition numbers as those of FEM. However in adaptive procedure, GSM produces much smaller condition numbers than FEM, which demonstrates the excellent stability of our present GSM.

4.5. L-shaped plate

Fig. 25 shows an L-shaped plate subjected to a tensile force $p=10$ in the horizontal direction. This is a classical problem to examine adaptive refinement schemes [5,14]. Since there is a singular point at the concave corner, an adaptive scheme is again required to identify the point of singularity and to refine the region around the node. This

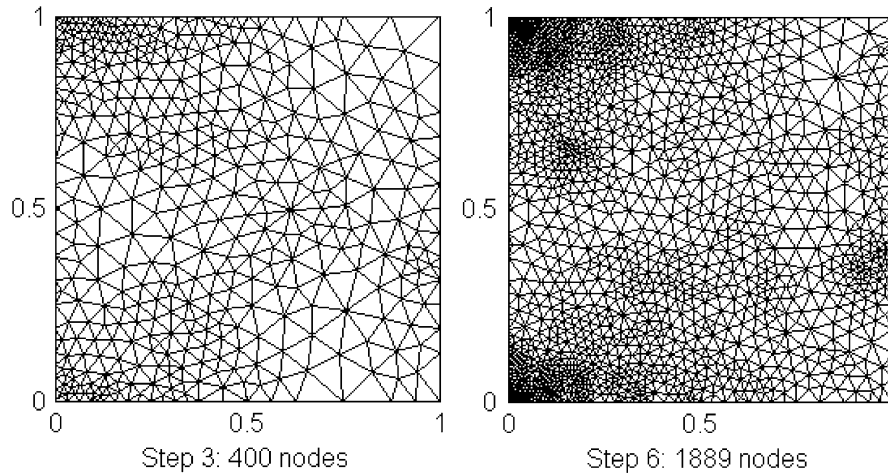


Fig. 19. Node distributions of adaptive refinement at the third and sixth steps for short cantilever plate.

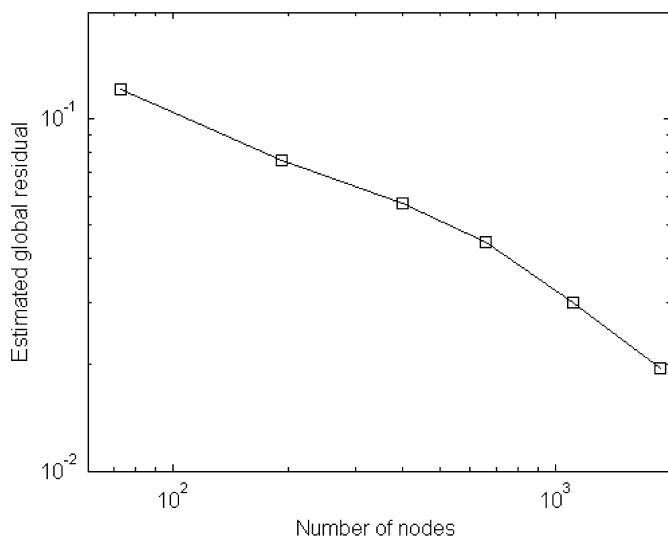


Fig. 20. Estimated global residual at each adaptive step for short cantilever plate.

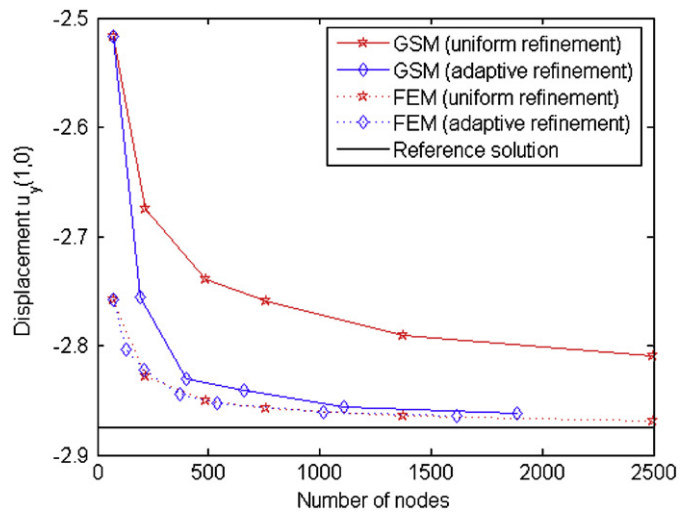


Fig. 21. Comparison of displacement $u_y(1,0)$ for short cantilever plate between GSM and FEM with uniform and adaptive refinements.

Table 10
Error norms of adaptive refinement for short cantilever plate using GSM

Step	1	2	3	4	5	6
No. of field nodes	73	193	400	657	1109	1889
$u_y(1,0)$						
Value	-2.5170	-2.7557	-2.8304	-2.8405	-2.8561	-2.8620
Error norm (%)	12.46	4.16	1.56	1.21	0.67	0.47
Energy						
Value	1.2867	1.3496	1.3647	1.3712	1.3751	1.3768
Error norm (%)	6.74	2.18	1.09	0.62	0.34	0.21

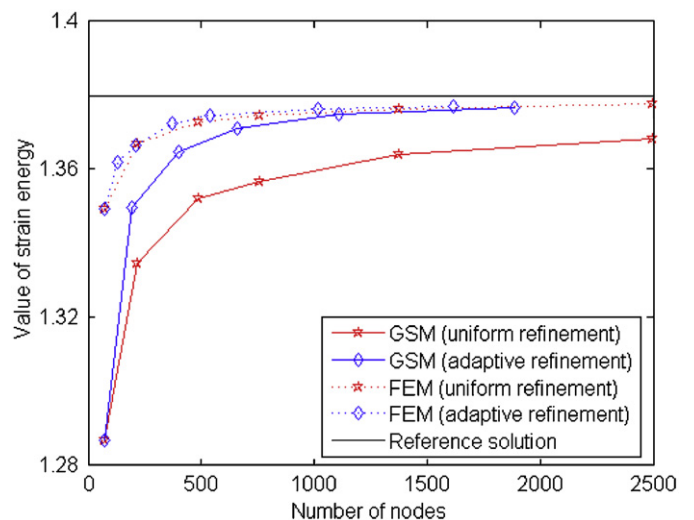


Fig. 22. Comparison of computed strain energy for short cantilever plate between GSM and FEM with uniform and adaptive refinements.

example is investigated as a plain stress problem. The geometry and material parameters used are $a = 5$, Young's modulus $E = 3.0 \times 10^7$ and Poisson's ratio $\nu = 0.3$. The boundary conditions are imposed as demonstrated in Fig. 25. As the exact solution for total strain energy is not available, a reference solution is obtained using linear FEM with a very fine mesh of 8732 nodes. The computed energy norm is 3.220292×10^{-2} , which is assumed as the reference solution.

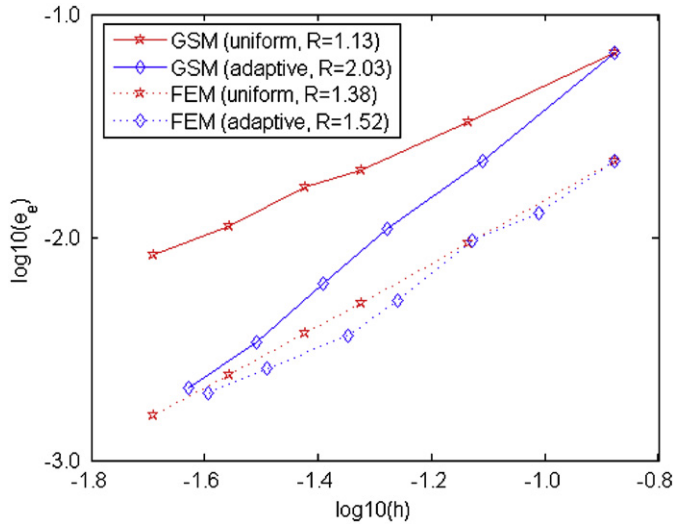


Fig. 23. Comparison of error and convergence rate in energy norm for short cantilever plate between GSM and FEM with uniform and adaptive refinements.

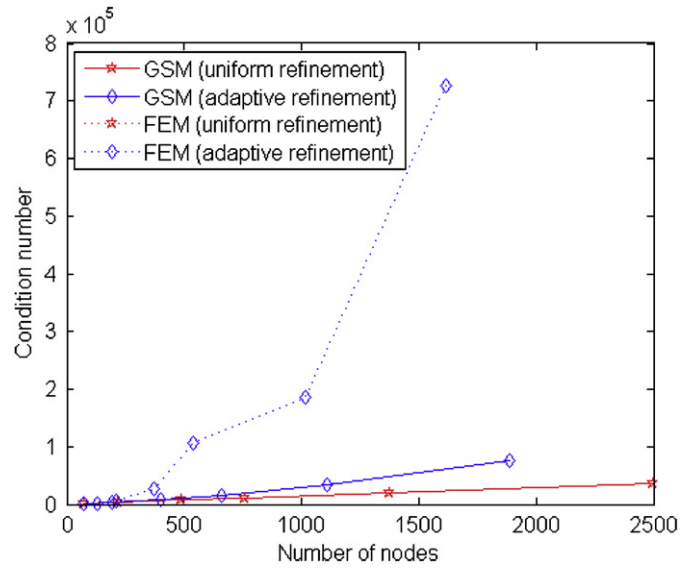


Fig. 24. Comparison of condition number of the coefficient matrix for short cantilever plate between GSM and FEM with uniform and adaptive refinements.

Table 11
Error norms of adaptive refinement for short cantilever plate using FEM

Step	1	2	3	4	5	6	7
No. of field nodes	73	127	209	370	541	1016	1614
$u_y(1,0)$							
Value	-2.7581	-2.8039	-2.8222	-2.8439	-2.8532	-2.8606	-2.8643
Error norm (%)	4.08	2.48	1.85	1.09	0.77	0.51	0.38
Energy							
Value	1.3492	1.3620	1.3664	1.3726	1.3747	1.3762	1.3770
Error norm (%)	2.21	1.29	0.97	0.52	0.36	0.26	0.20

We also start this example from 'uniform' refinement with 108, 369, 710, 1430, 2194 and 2948 nodes, respectively. Four selected distributions of nodes are shown in Fig. 26. The values of strain energy and its error norm are given in Table 12. The adaptive analysis starts with an initial mesh of 108 uniformly distributed nodes (see Fig. 26). The local refinement coefficient is predefined as $\kappa_1 = 0.025$, and the global residual tolerant coefficient is $\kappa_g = 0.05$. The adaptive refinement ends at the fifth step with 1489 irregular nodes in the problem domain. The node distributions of third and fifth steps are plotted in Fig. 27, which shows that the adaptive scheme is able to detect the singular point and refine the surrounding area accordingly. The calculated strain energy and its error norm for each adaptive step are presented in Table 13. From the comparison of energy norm between Tables 12 and 13, it is observed that the adaptive scheme converges to the reference solution much faster. The comparison of convergence rate in energy norm is shown in Fig. 28. Since the adaptive scheme can automatically refine the high stress region near the concave corner, it obviously accelerates the process of convergence, and hence improves the accuracy.

4.6. Mode-I crack problem

In this example, a Mode-I crack problem is considered for adaptive analysis. A square plate with sides of length $2a$ and a crack of length a is used, as shown in Fig. 29(a). The exact displacement and

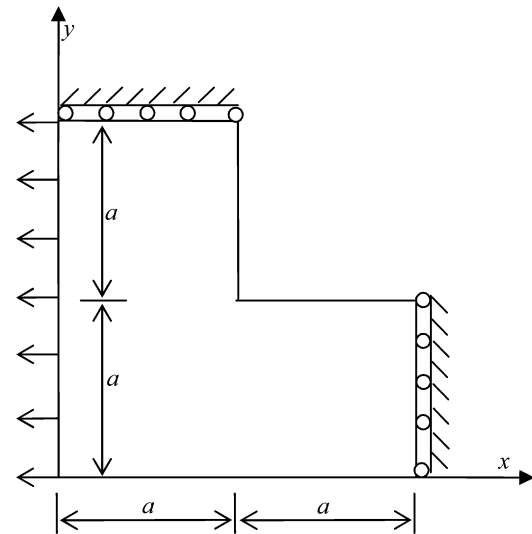


Fig. 25. L-shaped plate subjected to a tensile load in the horizontal direction.

stress solutions in the crack tip neighborhood are given by [30,31]

$$u_x = \frac{K_I}{2\mu} \sqrt{\frac{r}{2\pi}} \cos\left(\frac{\theta}{2}\right) \left[\kappa - 1 + 2 \sin^2\left(\frac{\theta}{2}\right) \right] \tag{46}$$

$$u_y = \frac{K_I}{2\mu} \sqrt{\frac{r}{2\pi}} \sin\left(\frac{\theta}{2}\right) \left[\kappa + 1 - 2 \cos^2\left(\frac{\theta}{2}\right) \right] \tag{47}$$

$$\sigma_{xx} = \frac{K_I}{\sqrt{2\pi r}} \cos\frac{\theta}{2} \left(1 - \sin\frac{\theta}{2} \sin\frac{3\theta}{2} \right) \tag{48}$$

$$\sigma_{yy} = \frac{K_I}{\sqrt{2\pi r}} \cos\frac{\theta}{2} \left(1 + \sin\frac{\theta}{2} \sin\frac{3\theta}{2} \right) \tag{49}$$

$$\sigma_{xy} = \frac{K_I}{\sqrt{2\pi r}} \sin\frac{\theta}{2} \cos\frac{\theta}{2} \cos\frac{3\theta}{2} \tag{50}$$

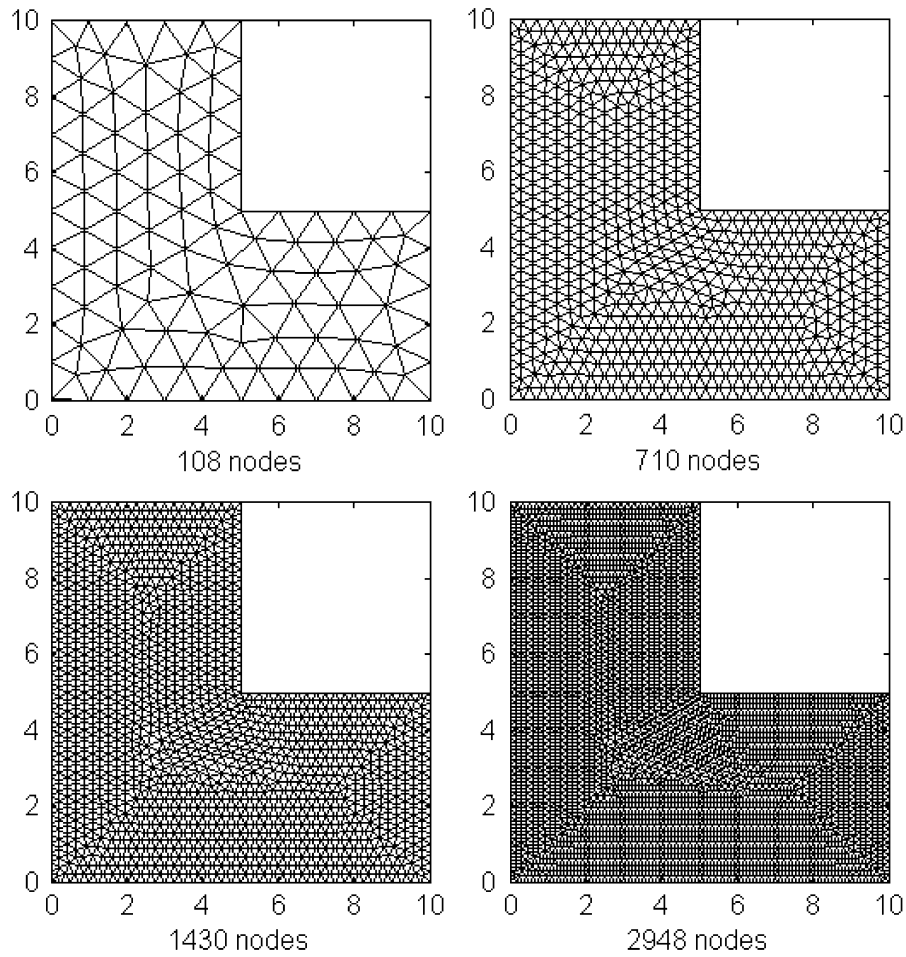


Fig. 26. Selected node distributions of uniform refinement for L-shaped plate.

Table 12

Error norms of uniform refinement for L-shaped plate

No. of field nodes	108	369	710	1430	2194	2948
Strain energy	3.5135E-2	3.3590E-2	3.3234E-2	3.2895E-2	3.2787E-2	3.2726E-2
Error norm (%)	9.11	4.31	3.20	2.15	1.81	1.62

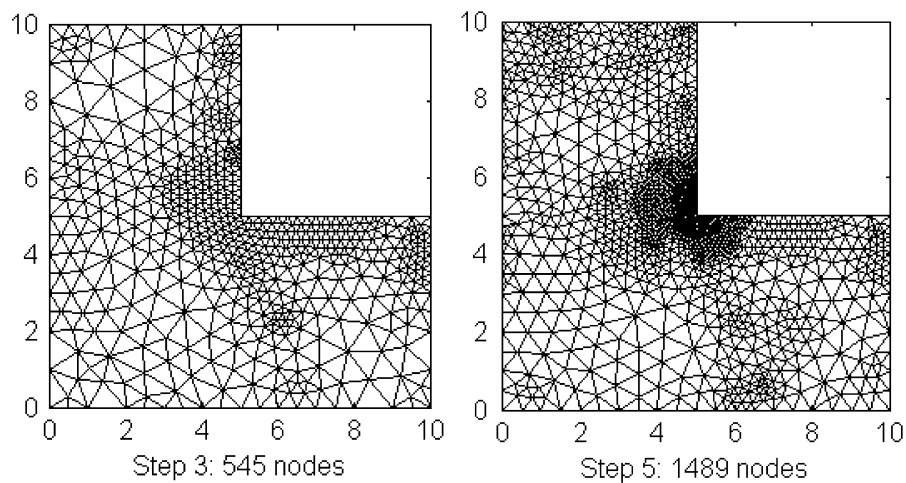


Fig. 27. Node distributions of adaptive refinement at the third and fifth steps for L-shaped plate.

where r is the distance from the crack tip and θ is the angle measured from the line of the crack. The stress intensity factor is prescribed as $K_I = \sqrt{2\pi} \mu$. μ is the shear modulus, and κ is defined as

$$\begin{aligned} \kappa &= \frac{3-\nu}{1+\nu} \quad \text{plane stress} \\ \kappa &= 3-4\nu \quad \text{plane strain} \end{aligned} \tag{51}$$

The problem is solved as a plain strain case with geometry and material parameters $a = 1, E = 3.0 \times 10^7, \nu = 0.3$. Due to the symmetry, only upper half of the plate is modeled, as shown in Fig. 29(b). To extend the above solutions to the whole studied domain, we impose on the square plate boundary (the upper, left and right edges)

Table 13
Error norms of adaptive refinement for L-shaped plate

	Step				
	1	2	3	4	5
No. of field nodes	108	242	538	817	1489
Strain energy	3.5135E-2	3.3378E-2	3.2824E-2	3.2515E-2	3.2346E-2
Error norm (%)	9.11	3.65	1.93	0.97	0.44

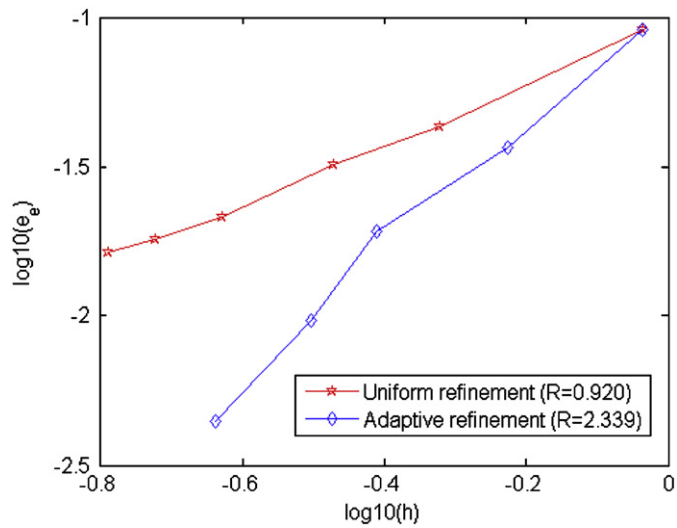


Fig. 28. Comparison of error and convergence rate in energy norm between uniform and adaptive refinements for L-shaped plate.

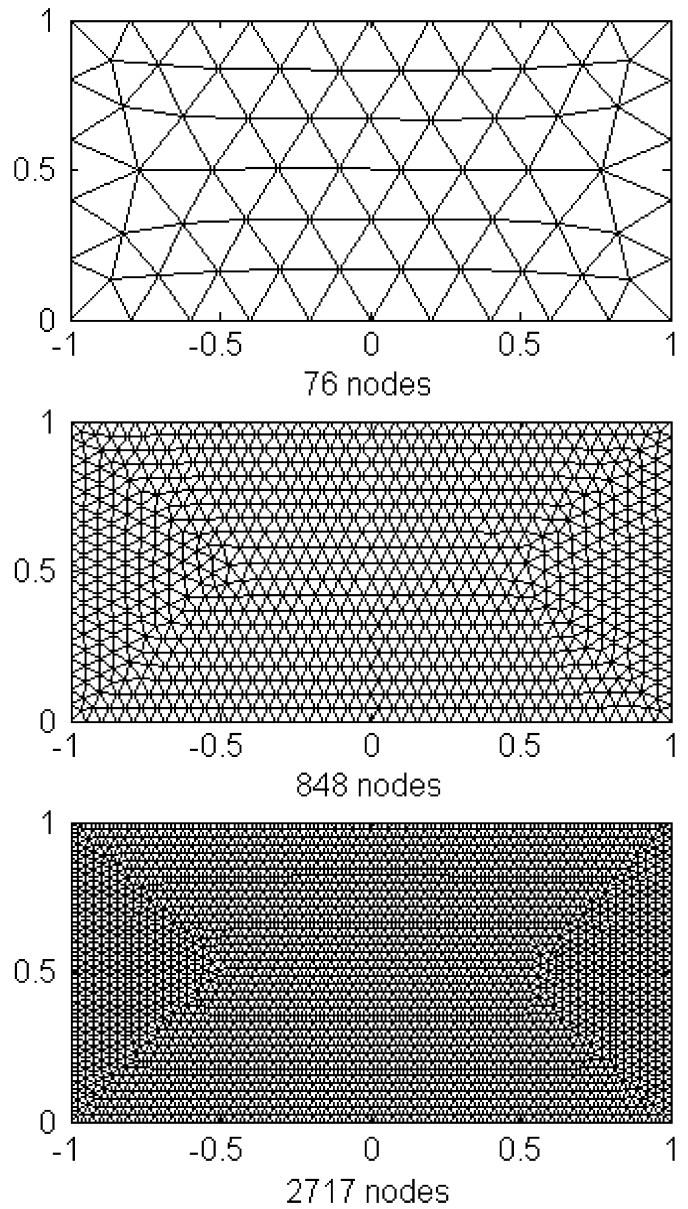


Fig. 30. Selected node distributions of uniform refinement for Mode-I crack problem.

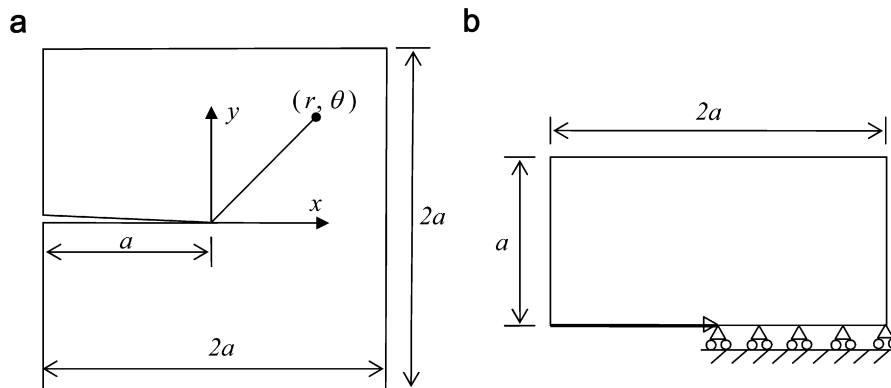


Fig. 29. Mode-I crack problem: (a) geometry and (b) half model with boundary conditions.

Table 14

Error norms of uniform refinement for Mode-I crack problem

No. of field nodes	76	252	542	848	1481	2717
Error norm of u_y (%)	49.68	29.03	21.13	17.37	13.85	10.64
Energy						
Value	2.8491E-4	2.9301E-4	2.9798E-4	3.0067E-4	3.0333E-4	3.0588E-4
Error norm (%)	9.45	6.88	5.30	4.44	3.60	2.79

the exact traction. Essential boundary conditions are applied as demonstrated in Fig. 29(b). Six distributions of uniform nodes, 76, 252, 542, 848, 1481 and 2717, are first investigated. Fig. 30 shows the selected node distributions. Similarly, the reference solution of strain energy, 3.146553×10^{-4} , is obtained using FEM (Gauss integration) with a very fine mesh of 9600 nodes based on analytical solutions of stress components. The computed displacement error in y -direction (u_y), strain energy and its error norm are presented in Table 14. It can be observed that both the displacement u_y and energy norm approach the exact (reference) solutions as nodes increase. However, the displacement error reduces very slowly due to the stress singularity near the crack tip. The error is still bigger than 10% with 2717 evenly distributed field nodes.

As shown in Fig. 30, the distribution of 76 field nodes is started for adaptive refinement. The local refinement coefficient is prescribed as $\kappa_1=0.05$ and the global residual tolerant coefficient is set as $\kappa_g=0.05$. As shown in Fig. 31, the adaptive analysis ends at the ninth step with 1144 extremely irregular nodes in the half plate domain. Due to stress concentration at the crack tip, a large number of nodes are inserted into the crack tip neighborhood (see Fig. 31). Table 15 presents displacement error in y -direction, energy and its error norm for each adaptive step. Compared with uniform refinement, the adaptive scheme is much more effective. The displacement error of u_y reduces as adaptive refinement goes. The comparisons of energy error and its convergence rate between uniform and adaptive refinements are presented in Fig. 32. It can be easily found that the GSM using adaptive scheme converges more than two times faster than uniform refinement.

4.7. Singular loading problem

To further examine the capability of our strong form GSM, a square solid subjected to a singular loading $P = 1$ at the center of the top edge is studied, as shown in Fig. 33. The solid is constrained in x and y directions along the left, right and bottom sides, respectively. This problem is solved as a plain strain case with geometry and material parameters as $a = 10$, $E = 1.0 \times 10^7$, $\nu = 0.3$.

This singular loading case is studied using the GSM with both uniform and adaptive models. For the uniform refinement, the problem domain is presented using 121, 625, 1681 and 3721 nodes (regular right triangular meshes), respectively, similarly as shown in Fig. 6 (regular left triangular meshes). For the adaptive procedure, 11 steps of adaptive refinement are performed with $\kappa_1 = 0.1$ and the nodal configuration at the sixth and eleventh steps is shown in Fig. 34. The figure shows that the present adaptive GSM can accurately catch the steep gradient of stresses and the occurrence of refinement properly concentrates around the point with singular loading. The displacements in x and y directions along the line $y = 5$ for both uniform and adaptive refinements are plotted in Figs. 35 and 36, respectively. For this problem, the reference solutions are obtained using adaptive FEM with a very fine mesh of 7431 nodes. In Fig. 37, the values of strain energy are presented for the results of uniform and adaptive refinements. The reference solution of the strain energy is 4.2812×10^{-3} . It can be concluded that the present GSM with

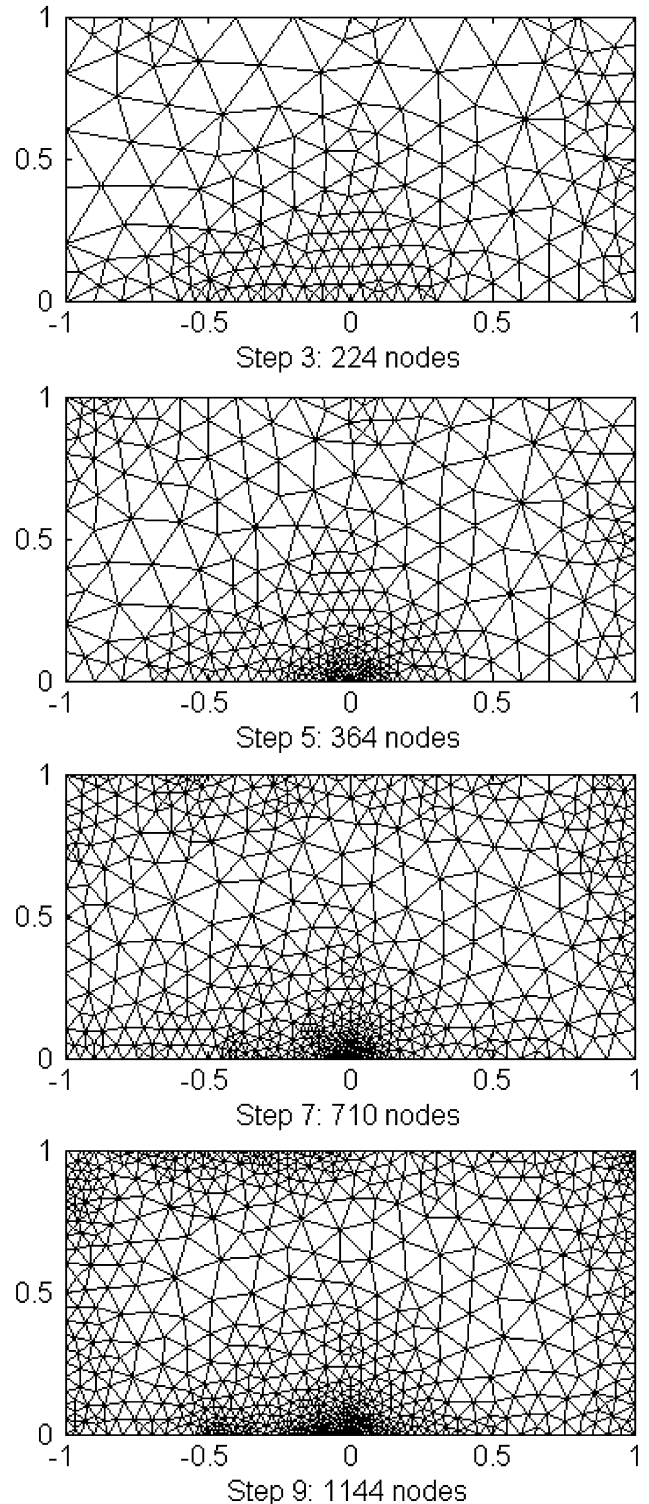


Fig. 31. Node distributions of adaptive refinement at the third, fifth, seventh and ninth steps for Mode-I crack problem.

Table 15
Error norms of adaptive refinement for Mode-I crack problem

Step	1	2	3	4	5	6	7	8	9
No. of field nodes	76	115	224	275	364	595	710	832	1144
Error norm of u_y (%)	49.68	30.18	15.74	13.15	12.92	7.63	6.27	4.53	2.18
Energy Value	2.8491E-4	2.9463E-4	3.0395E-4	3.0474E-4	3.0774E-4	3.1021E-4	3.1148E-4	3.1188E-4	3.1258E-4
Error norm (%)	9.45	6.36	3.40	3.15	2.20	1.41	1.01	0.88	0.66

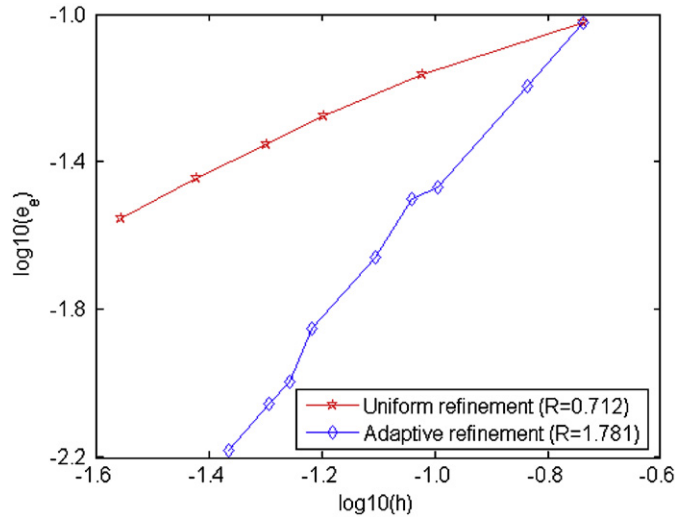


Fig. 32. Comparison of error and convergence rate in energy norm between uniform and adaptive refinements for Mode-I crack problem.

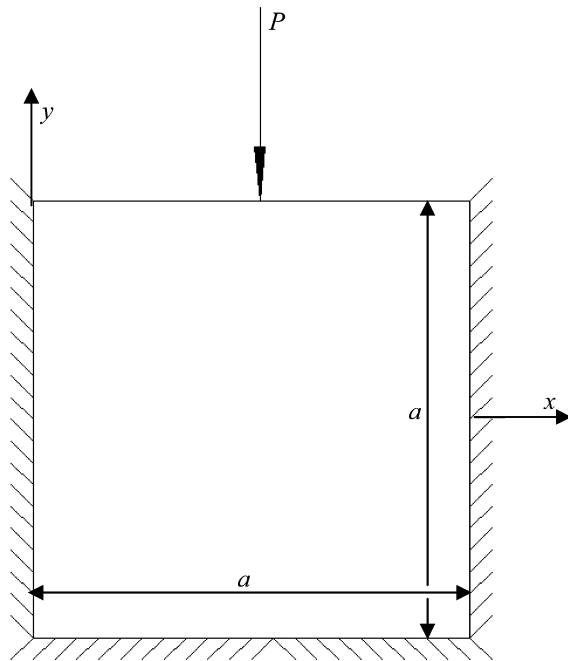


Fig. 33. A square solid subjected to a singular loading at the center of the top edge.

adaptive procedure can effectively produce reliable results for problems with high stress concentration, singular points and even singular loading.

5. Discussion and concluding remarks

In the current work, a gradient smoothing method (GSM) based on a strong form of governing equations is developed for solid mechanics problems: (1) In the present method, different types of smoothing domains are devised in a novel manner and used for approximation of derivatives. (2) The GSM can be used for mechanics problems with any arbitrarily irregular domains, singularities, and singular loading, which is very difficult for a strong form method. Both stability and accuracy have been demonstrated in comparison with the widely used FEM. The GSM has exhibited even much better than the FEM for adaptive analysis judging from the condition numbers. (3) Due to the excellent stability, the GSM is further extended to adaptive analysis and found effective. A simple yet robust residual based error indicator is adopted in our adaptive procedure. By approximating the residual of the governing equation in the domain, this error indicator can efficiently capture the region to be refined.

In the paper, our formulation is focused on 2D problems. The idea and general procedure of the GSM can, however, be generalized to 3D problems. The challenge will be in the construction of 3D smoothing domains and coding.

The present GSM has not yet formulated for solving the volume locking problem, for which especial techniques are needed. A large number of such techniques have been developed by many researchers for weak form methods, one of which is the so-called "selective" formulation. If the selective formulation is used in the GSM formulation with proper design of smoothing domains, the GSM should also be able to solve this type of locking problems. The authors believe that formulation towards this direction needs a lot more careful consideration and intensive investigation. Hence leave this topic for our further study.

From intensive numerical studies carried out on several benchmark problems with and without singularities, the following conclusions can be drawn:

1. The GSM can reproduce linear fields regardless of the types of boundary conditions (essential or natural). Hence, the solution will converge to any higher-order continuous fields as the field mesh is refined.
2. The study of numerical examples shows that the proposed GSM not only can obtain accurate and stable results but also is successful in the implementation for adaptive analysis with steady convergences.
3. For problems without singularity, even though there is no significant improvement in the convergence rate compared with the uniform refinement, our adaptive GSM can lead to solutions with much higher accuracy.
4. For problems where singular points exist, nearly optimal nodal distributions are generated automatically in the process of adaptive analysis. As a result, far less degrees of freedom are needed to achieve the desired accuracy compared with uniform refinement.
5. In summary, we conclude that the GSM is a stable, robust and reliable numerical method based on strong form formulation for adaptive analysis of solid mechanics problems.

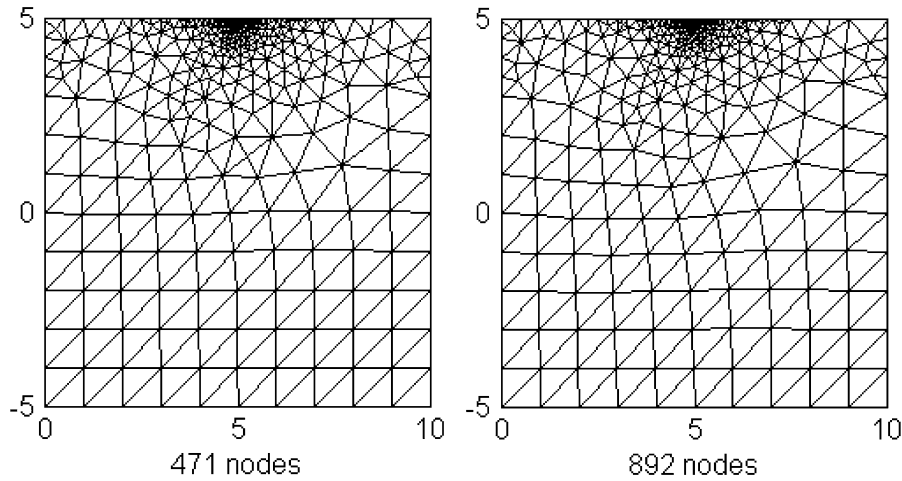


Fig. 34. Node distributions of adaptive refinement at the sixth and eleventh steps for singular loading problem.

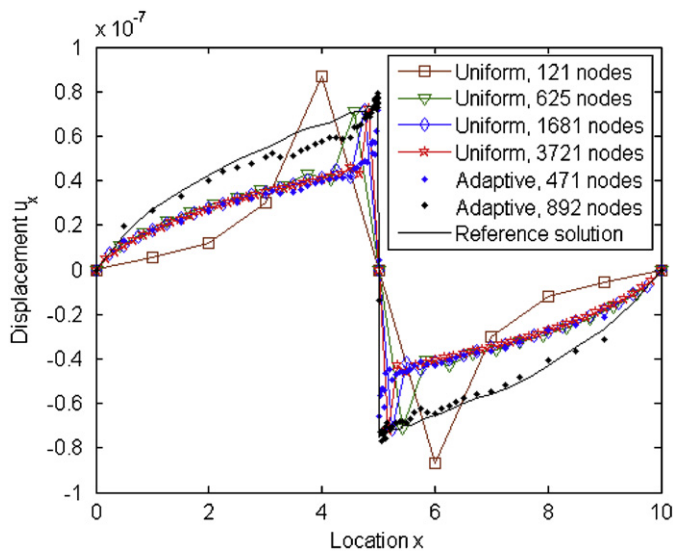


Fig. 35. Comparison of displacement $u_x(x,5)$ between uniform and adaptive refinements.

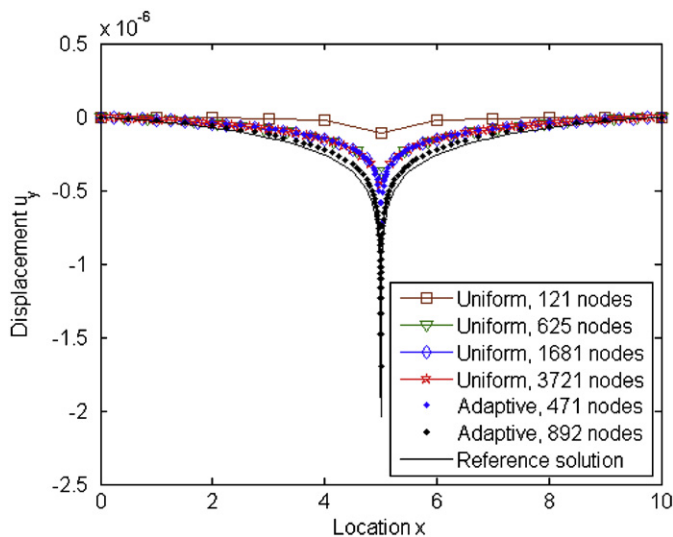


Fig. 36. Comparison of displacement $u_y(x,5)$ between uniform and adaptive refinements.

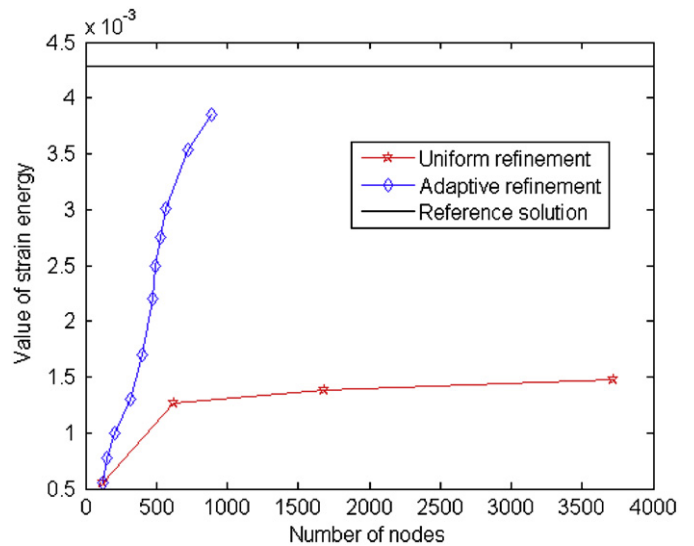


Fig. 37. Comparison of strain energy between uniform and adaptive refinements.

References

- [1] G.R. Liu, Meshfree Method: Moving Beyond the Finite Element Method, CRC Press, Boca Raton, FL, 2002.
- [2] G.R. Liu, Y.T. Gu, An Introduction to Meshfree Methods and Their Programming, Springer, Dordrecht, 2005.
- [3] T. Belytschko, Y. Krongauz, D. Organ, M. Fleming, P. Krysl, Meshless methods: an overview and recent developments, *Comput. Methods Appl. Mech. Eng.* 139 (1996) 3–47.
- [4] A. Huerta, A. Rodriguez-Ferran, P. Diez, J. Sarrate, Adaptive finite element strategies based on error assessment, *Int. J. Numer. Methods Eng.* 46 (1999) 1803–1818.
- [5] O.C. Zienkiewicz, R.L. Taylor, The Finite Element Method, fourth ed., McGraw-Hill, New York, NY, 1989.
- [6] M.S. Shephard, N.P. Weatherill (Eds.), Special issue on adaptive meshing, *Int. J. Numer. Methods Eng.* 32 (1991).
- [7] S.H. Lo (Ed.), Special issue on adaptive meshing, Part II, Finite elements in analysis and design 25.
- [8] C.A. Duarte, J.T. Oden, An h - p adaptive method using clouds, *Comput. Methods Appl. Mech. Eng.* 139 (1996) 237–262.
- [9] T.J. Liszka, C.A. Duarte, W.W. Tworzydlo, hp -Meshless cloud method, *Comput. Methods Appl. Mech. Eng.* 139 (1996) 263–288.
- [10] H.J. Chung, G.H. Lee, C.K. Choi, Adaptive nodal generation with the element-free Galerkin method, *Struct. Eng. Mech.* 10 (2000) 635–650.
- [11] L. Gavete, S. Falcon, A. Ruiz, An error indicator for the element free Galerkin method, *Eur. J. Mech. A-Solids* 20 (2001) 327–341.

- [12] C.K. Lee, C.E. Zhou, On error estimation and adaptive refinement for element free Galerkin method, Part II: Adaptive refinement, *Comput. Struct.* 82 (2004) 429–443.
- [13] S.H. Park, K.C. Kwon, S.K. Youn, A posteriori error estimates and an adaptive scheme of least-squares meshfree method, *Int. J. Numer. Methods Eng.* 58 (2003) 1213–1250.
- [14] G.R. Liu, B.B.T. Kee, C. Lu, A stabilized least-squares radial point collocation method (LS-RPCM) for adaptive analysis, *Comput. Methods Appl. Mech. Eng.* 195 (2006) 4843–4861.
- [15] E. Onate, F. Perazzo, J. Miquel, A finite point method for elasticity problems, *Comput. Struct.* 79 (2001) 2153–2163.
- [16] N.R. Aluru, A point collocation method based on reproducing kernel approximations, *Int. J. Numer. Methods Eng.* 47 (2000) 1083–1121.
- [17] D.W. Kim, Y. Kim, Point collocation methods using the fast moving least-square reproducing kernel approximation, *Int. J. Numer. Methods Eng.* 56 (2003) 1445–1464.
- [18] D.W. Kim, W.K. Liu, Maximum principle and convergence analysis for the meshfree point collocation method, *SIAM J. Numer. Anal.* 44 (2006) 515–539.
- [19] T. Liszka, J. Orkisz, Finite difference method at arbitrary irregular grids and its application in applied mechanics, *Comput. Struct.* 11 (1979) 88–95.
- [20] G.R. Liu, J. Zhang, H. Li, K.Y. Lam, B.B.T. Kee, Radial point interpolation based finite difference method for mechanics problems, *Int. J. Numer. Methods Eng.* 68 (2006) 728–754.
- [21] J.S. Chen, C.T. Wu, S. Yoon, Y. You, A stabilized conforming nodal integration for Galerkin mesh-free methods, *Int. J. Numer. Methods Eng.* 50 (2001) 435–466.
- [22] D. Shepard, A two dimensional interpolation function for irregularly spaced points, in: *Proceedings of ACM National Conference*, 1968, pp. 517–524.
- [23] G.R. Liu, J. Zhang, K.Y. Lam, et al., A gradient smoothing method (GSM) with directional correction for solid mechanics problems, *Comput. Mech.* 41 (2008) 457–472.
- [24] S.V. Patankar, *Numerical Heat Transfer and Fluid Flow*, McGraw-Hill, New York, NY, 1980.
- [25] T. Barth, *Numerical methods for conservation law on structured and unstructured meshes*, VKI 2003 Lecture Series, 2003.
- [26] B.B.T. Kee, G.R. Liu, C. Lu, A regularized least-squares radial point collocation method (RLS-RPCM) for adaptive analysis, *Comput. Mech.* 40 (2007) 837–853.
- [27] S.P. Timoshenko, J.N. Goodier, *Theory of Elasticity*, third ed., McGraw-Hill, New York, NY, 1970.
- [28] C. Johnson, P. Hansbo, Adaptive finite element methods for small-strain elastoplasticity, in: D. Besdo, E. Stein (Eds.), *Finite Inelastic Deformations—Theory and Applications*, Springer, Berlin, 1991.
- [29] H. Steeb, A. Maute, E. Ramm, Goal-oriented error estimation in solid mechanics, in: E. Stein (Ed.), *Error-controlled Adaptive Finite Elements in Solid Mechanics*, Wiley, UK, 2002.
- [30] N. Perrone, H. Liebowitz, D. Mulville, W. Plikey, *Fracture Mechanics*, University Press of Virginia, Charlottesville, 1978.
- [31] T.L. Anderson, *Fracture Mechanics: Fundamentals and Applications*, first ed., CRC Press, Boca Raton, 1991.